Mapping landslide surface displacements with time series SAR interferometry by combining persistent and distributed scatterers: A case study of Jiaju landslide in Danba, China

Jie Dong[a], Lu Zhang[a,b,*], Minggao Tang[c], Mingsheng Liao[a,b], Qiang Xu[c], Jianya Gong[a,b,d], Meng Ao[a]

[a] State Key Laboratory of Information Engineering in Surveying, Mapping, and Remote Sensing, Wuhan University, Wuhan, China
[b] Collaborative Innovation Center for Geospatial Technology, Wuhan University, Wuhan, China
[c] State Key Laboratory of Geohazard Prevention and Geoenvironment Protection, Chengdu University of Technology, Chengdu, China
[d] School of Remote Sensing and Information Engineering, Wuhan University, Wuhan, China

ARTICLE INFO

ABSTRACT

InSAR technology provides a powerful tool to detect potentially unstable slopes across wide areas and to monitor surface displacements of a single landslide. However, conventional time series InSAR methods such as persistent scatterer interferometry (PSI) and small-baseline subset (SBAS) can rarely identify sufficient measurement points (MPs) in mountainous areas due to decorrelations caused by steep terrain and vegetation coverage. In this study, we developed a new InSAR approach, coherent scatterer InSAR (CSI), to map landslide surface displacements in the radar line-of-sight (LOS) direction by combining persistent scatterers (PS) and distributed scatterers (DS). The key ideas of CSI include the employment of the generalized likelihood ratio (GLR) test for the identification of statistically homogeneous pixels (SHPs) and the use of the phase linking algorithm to estimate optimal phase for each DS pixel. The joint exploitation of PS and DS targets dramatically increases the spatial density of MPs, which makes the phase unwrapping more reliable. To demonstrate the effectiveness of the CSI approach, we applied it to retrieve the historical displacements of the Jiaju landslide in Danba County of southwest China using 19 L-band ALOS PALSAR images (2006–2011) and nine C-band ENVISAT ASAR images (2007–2008). Multiple comparisons clearly illustrated the big advantages of CSI over PSI and SBAS in mapping landslide displacements with more details owing to much higher (> 10 times) MP density. Furthermore, the superiority of L-band SAR data over C-band for landslide investigation in rural environments was confirmed. Quantitative validation of the CSI results for PALSAR data against in-situ GPS measurements suggested an accuracy of about 10.5 millimeters per year (mm/year) in terms of root mean square error (RMSE). Afterwards, the spatial-temporal characteristics of the Jiaju landslide surface displacements were summarized, with a new upper boundary for the active northern part delineated. Particularly, the northern part of the landslide moved faster than the southern part, exhibiting a maximum LOS displacement rate of around 120 mm/year. Subsequently, the fluvial erosion by the Dajinchuan River was identified as the predominant impact factor for the instability of the Jiaju landslide. Finally, the major problems and challenges for the application of CSI method were discussed, and the conclusions were given.

1. Introduction

SAR interferometry (InSAR) detects and measures ground surface deformations from multiple platforms at high precision with wide coverages, high resolutions, and frequent acquisitions (Bamler and Hartl, 1998; Gabriel et al., 1989; Massonnet and Feigl, 1998; Rosen et al., 2000; Simons and Rosen, 2007). The first successful application of differential InSAR (DInSAR) in monitoring the Saint-Etienne-de-Tinée landslide opened up a new capability for landslide measurement (Fruneau et al., 1996). However, DInSAR is limited by temporal and geometrical decorrelations (Zebker and Villasenor, 1992) and atmospheric delay anomalies (Massonnet and Feigl, 1998). Over the past two decades, time series InSAR techniques were developed to overcome these limitations by focusing on coherent radar targets instead of the ensemble of image pixels (Berardino et al., 2002; Ferretti et al., 2001; Hooper, 2008; Hooper et al., 2004; Iglesias et al., 2015; Lanari et al.,

2004; Mora et al., 2003). Time series InSAR techniques can be grouped into two main categories: persistent scatterer (PS) and distributed scatterer (DS) according to the scattering mechanisms of the ground targets used.

In general, PS approaches focus on point-like coherent targets dominated by a single scatterer. These targets exhibit highly stable backscattering behaviour and usually correspond to artificial reflectors, man-made structures, or bare rocks. PS approaches take a single-master strategy and only produce $N - 1$ interferograms from N single-look complex (SLC) images co-registered to a common master image. Typical algorithms include PSInSAR™ (Ferretti et al., 2001), IPTA (Werner et al., 2003), StaMPS/PSInSAR (Hooper, 2008; Hooper et al., 2004), SPINUA (Bovenga et al., 2006; Bovenga et al., 2004), STUN (Kampes, 2006), SPN (Crosetto et al., 2008; Kuehn et al., 2010), PSP (Costantini et al., 2008; Costantini et al., 2014), and GEOS-PSI (Ng et al., 2012).

In contrast to PS methods, DS approaches employ distributed targets that contain lots of small random scatterers without one being dominant (Bamler and Hartl, 1998). Distributed targets such as bare soil, sparsely vegetated or desert lands, are typically found in rural environments. In DS approaches, M $(N - 1 < M < N(N - 1)/2)$ multi-master interferograms with short spatial-temporal baselines are generated. Classical DS algorithms include SBAS (Berardino et al., 2002; Casu et al., 2006; Lanari et al., 2004; Schmidt and Bürgmann, 2003), QPS (Perissin and Wang, 2012), π-RATE (Biggs et al., 2007), and TCPInSAR (Zhang et al., 2011; Zhang et al., 2012).

The new-generation time series InSAR techniques were developed to further maximize the spatial sampling of deformation signal over rural regions. One is the multi-temporal InSAR (MTInSAR) that integrates StaMPS/PSInSAR and SBAS methods (Hooper, 2008). Unlike the MTInSAR algorithm, SqueeSAR™ jointly processes PS and DS targets to retrieve the deformation signal (Ferretti et al., 2011). Particularly, this method makes full use of all the possible combinations, i.e. $N(N - 1)/2$ interferograms, to pre-process DS targets, without limitation on temporal or geometrical baselines. Recently, some extended algorithms were developed following the principle of SqueeSAR™, such as JSInSAR (Lv et al., 2014), CAESAR (Fornaro et al., 2015), PD-PSInSAR (Cao et al., 2015), and GEOS-ATSA (Du et al., 2016; Ge et al., 2014; Ng et al., 2015).

The time series InSAR techniques have been widely applied to detect potentially unstable slopes and monitor local-scale landslides (Colesanti et al., 2003; Colesanti and Wasowski, 2006; Confuorto et al., 2017; Costantini et al., 2017; Di Martire et al., 2017; Eriksen et al., 2017; Hilley et al., 2004; Shi et al., 2016; Wasowski and Bovenga, 2014). However, there is few reported work combining PS and DS targets to investigate landslides. In addition, in SqueeSAR™, a key step is to identify SHP, implemented through the embedded DespecKS procedure (Ferretti et al., 2011). DespecKS employs the Kolmogorov–Smirnov (KS) test to discriminate if two amplitude series belong to the same statistical distribution (Stephens, 1970). Nevertheless, the KS test needs a large number of SAR images ($N > 20$) to robustly support the null hypothesis that the two samples were drawn from the same population (Jiang et al., 2015). Meanwhile, the Broyden-Fletcher-Goldfarb-Shanno (BFGS) algorithm adopted to solve the problem of optimal phase estimation in SqueeSAR™ has a very high computation time cost (Fletcherwrited, 1981).

In this study, we propose a new approach, named coherent scatterer InSAR (CSI), to investigate landslides by combining PS and DS targets. The PS targets are pre-processed using the conventional procedure (Hooper et al., 2004), while the DS pre-processing differs from SqueeSAR™ in two aspects. First, if the number of available images is less than 20, the generalized likelihood ratio (GLR) test is adopted as an alternative of the KS test for SHP identification. Second, a phase linking approach is implemented to estimate the optimal interferometric phase values from the complex coherence matrix for each DS target (Monti Guarnieri and Tebaldini, 2008). The pre-processed PS and DS scatterers are combined to create the Delaunay triangular network for phase

unwrapping and the deformation is estimated using standard time series analysis procedure. The combination of PS and DS significantly increases the spatial density of MPs, and thus makes phase unwrapping more robust.

The CSI method was applied to study the Jiaju landslide in Danba County, China using archived ALOS PALSAR and ENVISAT ASAR datasets. Comparisons among the results of CSI, StaMPS/PSInSAR (PSI in abbreviation) and SBAS were carried out to demonstrate the advantages of the CSI method. The deformation rates measured by the two SAR datasets were compared for the evaluation of cross-sensor consistency. The CSI results derived from PALSAR datasets were quantitatively validated using in-situ GPS measurements. Furthermore, the spatial-temporal characteristics of the Jiaju landslide deformation were analyzed, and the driving factors for the landslide instability were sorted out. Finally, discussions and conclusions were given.

2. Study area

2.1. Geological setting

Danba, a county of Garzê Tibetan Autonomous Prefecture, is situated in Sichuan Province, southwest China. Danba County is located between national highways G317 and G318, with provincial roads S211 and S303 passing through, as seen in Fig. 1. The Dajinchuan River drains into the famous Dadu River at Danba County.

The study area lies in the east margin of the Qinghai-Tibet Plateau and belongs to the Minshan-Qionglai Alps. It is characterized by steep terrains and alpine valleys with the altitude varying from 1700 m to 5520 m above sea level (a.s.l.). Many hillsides are mantled by superficial deposits, which also include considerable amounts of rough materials from rock falls and rockslides. There is a wide variety of metamorphic and tectonic deformations in this complicated geological area. As a key forest area in southwest China, Danba has a range of dense forest vegetation types, but short shrubs cover approximately 46% of the area.

Located in the Qinghai-Tibet plateau monsoon climate zone, Danba has moderate annual rainfall that is concentrated in the summer months, with an average annual rainfall of 594 mm. Consequently, strong polymetamorphism and tectonic movements, rock falls, landslides and debris flows break out frequently and widely in the area (Huang, 2009). Human activities, road construction, building expansion, and irrigation, also cause new landslides or reactivate old landslides. In the last decade, numerous geological disasters, especially landslides, occurred in Danba County, causing enormous economic losses and loss of life and property (Chen et al., 2005; Deng et al., 2017; Yin et al., 2008).

2.2. Jiaju landslide

The Jiaju village, not far away from Danba town, is well known for its special Tibetan-style buildings. It is rated as one of the most beautiful Chinese villages. The flourishing tourism promotes the rapid expansion of Jiaju village to several times of its original size in the last two decades. Unfortunately, it is located on a giant slow-moving landslide as shown in Fig. 2. The background image is a shaded high-resolution digital surface model (DSM) at a resolution of 0.2 m acquired by UAV aerial photogrammetry in March 2017.

The Jiaju landslide looks like a capital M in shape with the boundary outlined by the black lines in Fig. 2. It can be divided into northern and southern parts, with the slope ranging from 10° to 32° (Yin et al., 2010). Jiaju landslide covers an area of 1.2 km², with a length of 1200 m in EW direction and a width of 1000 m in the SN direction. According to geophysics exploration and borehole drilling, the landslide body has a thickness of 20–90 m and it is comprised of detritus earth and boulders with some silt clay, as shown in Fig. 3. Its volume is estimated to be about 26 million m³.
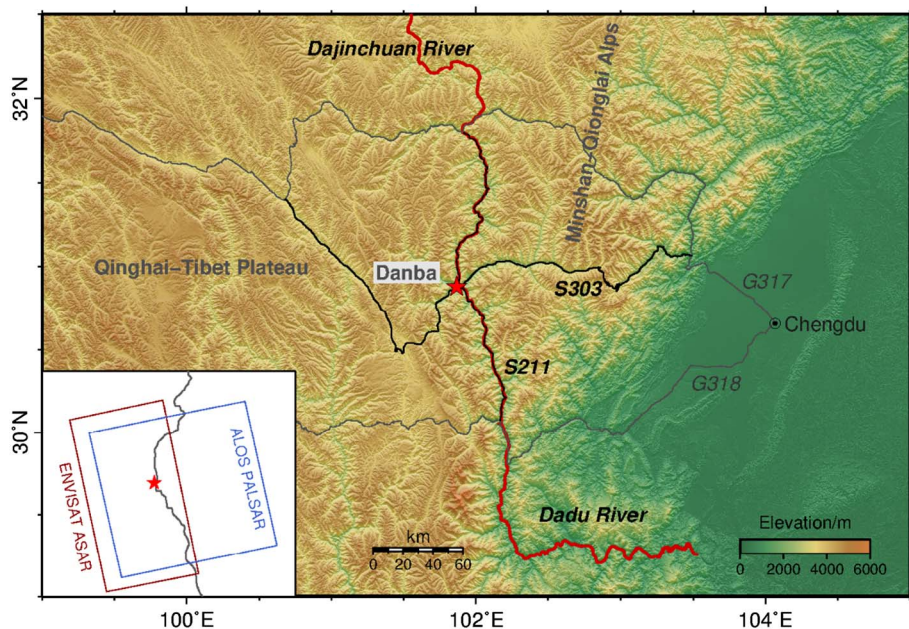
Fig. 1. The location of the study area and the image coverages of ALOS PALSAR and ENVISAT ASAR data stacks. The background is the shaded ASTER GDEM of 1 arcsecond resolution.

There is a major fracture at the center of the landslide, about 30 m in length, 5–15 cm in width, and 30–60 cm in depth. Many houses with cracks can be found along the fracture belt. During the rainy season, small surface fissures appear in the rear part of the landslide, while several perennial and manmade ditches are found along the slope,

penetrating into the earth surface mass. A geological survey showed that the northern part of the Jiaju landslide moves faster than the southern part and the rear slides slower than the front (Deng et al., 2011; Yin et al., 2008).

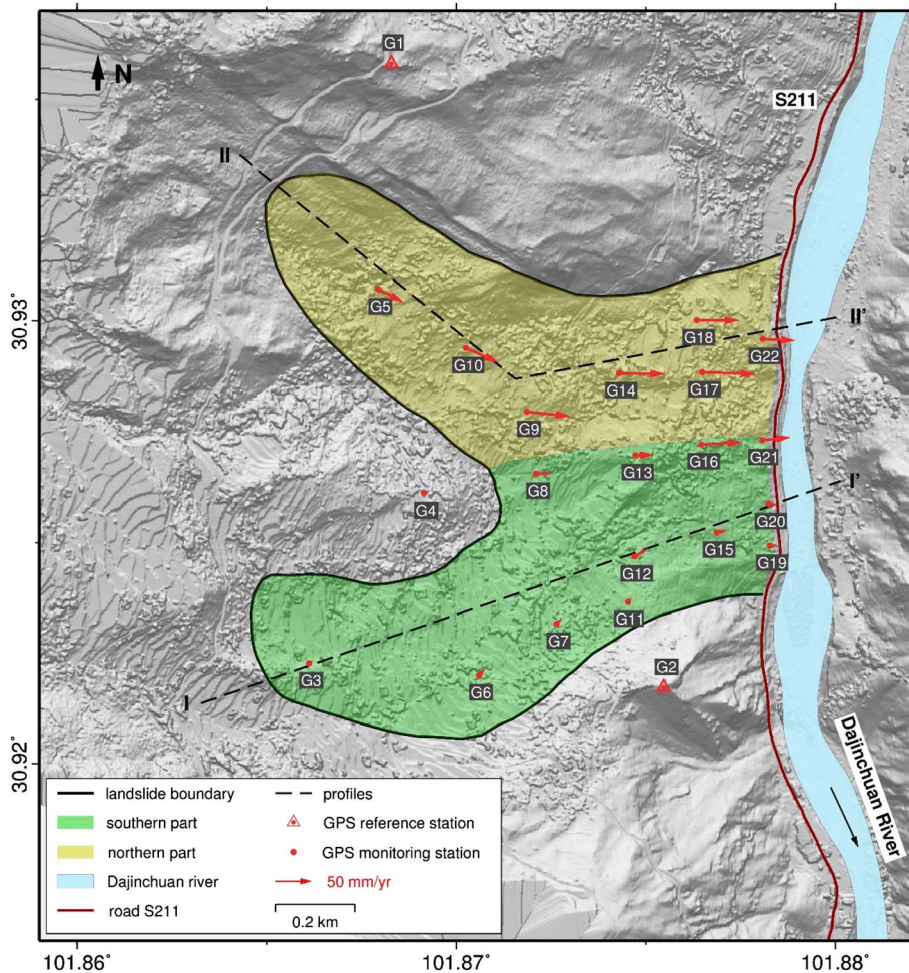A photo taken in July 2008 gives an overall perspective view of the

Fig. 2. Planar overview of the Jiaju landslide. The red arrows indicate the horizontal deformation rates of the 20 GPS monitoring stations. The background is the shaded DSM produced in March 2017. The landslide boundary is defined by Yin et al. (2010). (For interpretation of the references to color in this figure legend, the reader is referred to the web version of this article.)
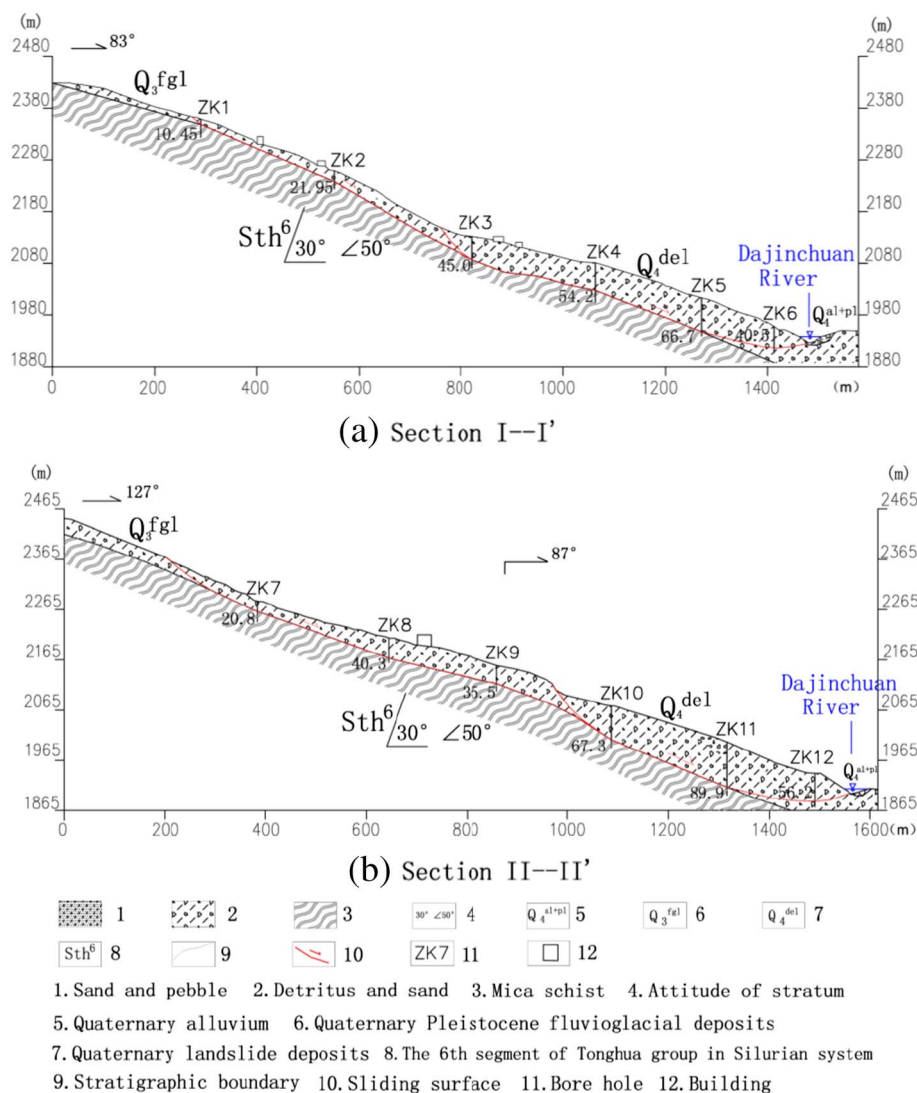
Fig. 3. Engineering geological profiles of the Jiaju landslide. (a) section I–I', (b) section II–II'. The location of the profiles is indicated by the black dashed lines in Fig. 2.

Jiaju landslide, as shown in Fig. 4(a). The photo in Fig. 4(b) taken in May 2015 illustrates the damage to the S211 roadway and slope foot induced by erosion from the Dajinchuan River. A crack with a width of about 10 cm was found in the road at the rear of Jiaju landslide, as shown in Fig. 4(c).

3. Data

3.1. Satellite SAR datasets

Archived SAR datasets collected by the ALOS and ENVISAT satellites were used to map the displacements of the Jiaju landslide. A total of 19 L-band ALOS PALSAR level 1.0 raw data products were acquired from path 478 between December 2016 and January 2011, and nine C-band ENVISAT ASAR SLC images were captured from track 455 during a shorter period from August 2007 to June 2008. Both datasets were acquired in ascending right-looking geometry but with different look angles (34° for PALSAR and 38° for ASAR). The detailed acquisition parameters for these two SAR data stacks are listed in Table 1, with their coverages shown in the inset map of Fig. 1.

Fig. 5 illustrates the different interferometric combinations of PALSAR images for PSI, SBAS, and DS pre-processing. The black dots represent SAR observations and the lines linking the dots indicate interferometric data pairs. The horizontal axes refer to the observation dates while the vertical axes correspond to the normal baselines.

In addition, since a reference DEM is required to estimate and remove the topographic phase in the two-pass DInSAR processing, the ASTER GDEM of 1 arc-second resolution with overall estimated vertical accuracies between 10 and 25 m in terms of root mean square error (RMSE) was also collected (Fujisada et al., 2005), as shown in Fig. 1.

3.2. GPS measurements

A GPS observation network was set up in August 2006, including 20 monitoring stations deployed over the landslide body and two reference stations installed on the stable bedrock nearby (Yin et al., 2010). The spatial distribution of all the GPS stations is shown in Fig. 2. The red arrows indicate the directions and magnitudes of the horizontal displacement rates of GPS monitoring stations. The stations G1 and G2 located outside the landslide boundary are selected as reference points, and assumed to be stable.

The GPS observation data has been collected from August 2006 to December 2013 with four epochs per year, which completely covers the acquisition times of both PALSAR and ASAR datasets. The dual-frequency Trimble 5700 GPS receivers with a 15 second interval were used and the elevation mask was set as 10° for all stations. For the monitoring stations, the length of surveying sessions was 24 h, while 3–6 days for the reference stations. The GAMIT/GLOBK software was employed to process the GPS observation data. The epochs in August 2006 and September 2007 were dropped due to abnormal observations
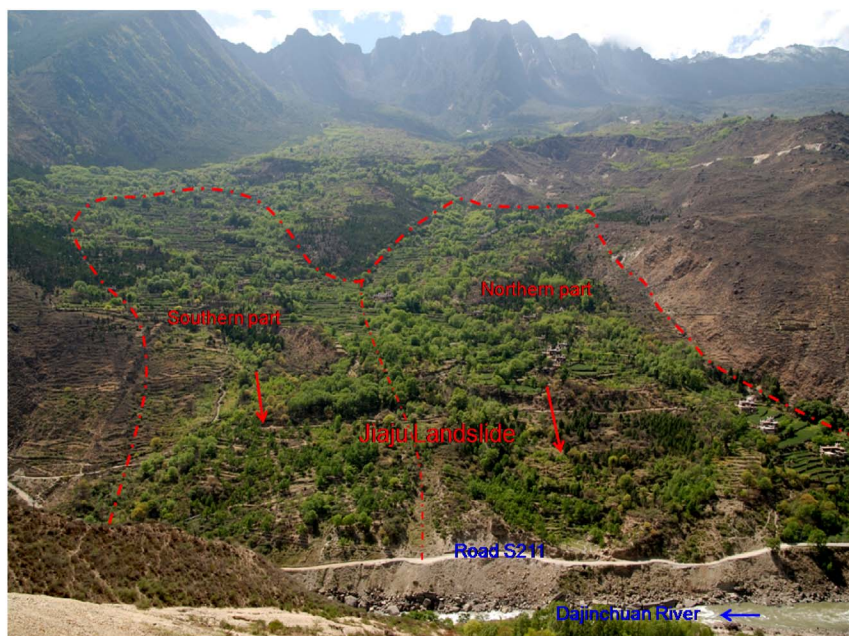
Fig. 4. The onsite photos of the Jiaju landslide. (a) The overall view shows the dense vegetation coverage (July 2008), (b) the slope foot was damaged by river erosion and bank was reinforced with many arrayed gabions (May 2015), (c) a crack in the road at the rear of the northern part (April 2017).

Table 1
The acquisition parameters of PALSAR and ASAR data used in our study.

SAR sensor	ALOS PALSAR	ENVISAT ASAR
Orbit direction	Ascending	Ascending
Microwave band (wavelength)	L-band (23 cm)	C-band (5.6 cm)
Resolution	10 m	20 m
Repeat cycle	46 days	35 days
Look angle	34°	38°
No. of images	19	9
Temporal coverage	Dec 2006–Jan 2011	Aug 2007–Jun 2008

at all stations.

4. Methodology

In this article, a new time series InSAR analysis procedure named CSI is proposed to measure landslide deformation by combining persistent and distributed scatterers. The CSI method consists of three steps, i.e. PS pre-processing, DS pre-processing, and joint analysis of PS and DS, as shown in the flowchart of Fig. 6.

As shown in Fig. 6, the PS pre-processing focuses on the selection of PS targets, while the DS pre-processing identifies the DS targets and

estimates their optimal phases. The selected PS and DS targets are jointly processed to retrieve the deformation measurements. In the following sections each of the three steps will be explained in detail.

4.1. PS pre-processing

In the first step, the same procedure used in StaMPS is employed to select PS points based on amplitude and phase information (Hooper et al., 2007), as shown in the block on the left side of Fig. 6. Since amplitude stability can be considered as an accurate proxy of phase stability when the coherence is high, we can apply amplitude dispersion index (ADI) to initially select PS candidates (Ferretti et al., 2001). The ADI of a certain pixel, denoted as D_A, is defined as:

$$D_A = \frac{\sigma_A}{\mu_A} \tag{1}$$

where μ_A and σ_A are the mean and standard deviation of a series of amplitude values for one pixel, respectively. Only the pixels exhibiting ADI values under a given threshold (typically < 0.4) are considered as PS candidates (PSCs).

Phase stability is then analyzed for each PSC under the assumption that the deformation signal is spatially correlated. A band-pass filter is employed to filter the phase observations of neighboring PSCs in the
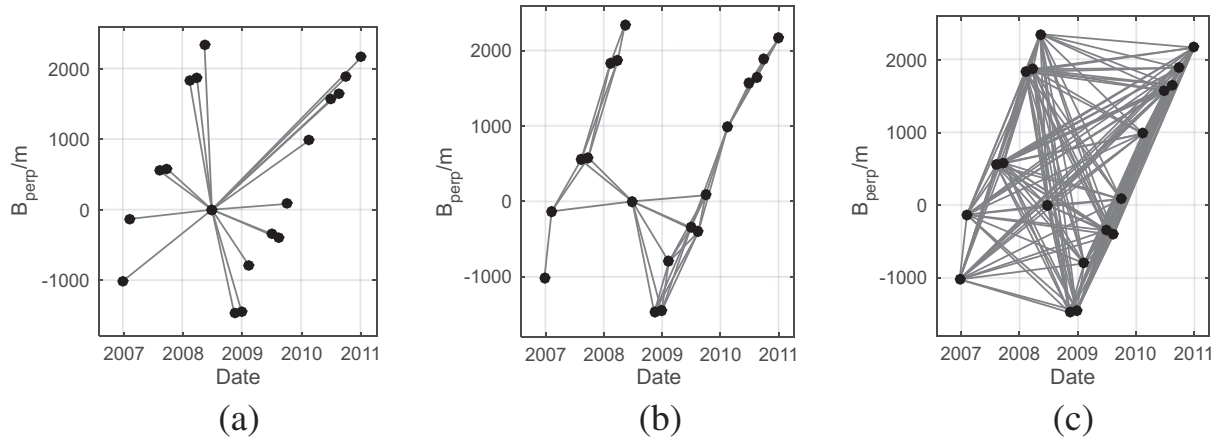
Fig. 5. The different interferometric combinations of PALSAR datasets for (a) PSI, (b) SBAS, and (c) DS pre-processing.

frequency domain to get the residual phase noise (Hooper et al., 2007). A phase stability indicator is defined as the temporal coherence γ in the following mathematic expression:

$$\gamma = \frac{1}{N} \left| \sum_{i=1}^{N} e^{j\varphi_{n,i}} \right| \tag{2}$$

where N is the number of images, $\varphi_{n,i}$ is the estimated residual phase noise of ith SLC image. The value of γ is estimated through an iterative strategy, and the procedure ends at convergence when the RMS change in γ is less than a given threshold. Only the PS candidates with high γ value are kept. Optionally, the phase stability indicator can be re-estimated on the selected PS pixels to refine the PS selection. The finally selected PS pixels with their original phase values are used for further time series analysis.

4.2. DS pre-processing

A more complicated procedure is required for pre-processing of DS targets, which consists of two steps, i.e. SHP identification and optimal phase estimation, as shown in the block on the right side of Fig. 6. The details are given below.

4.2.1. SHP identification

When the available SAR images are sufficient to evaluate the amplitude sample (typically > 20), a KS test is applied to identify the SHP pixels (Parizzi and Brcic, 2011). However, when the number of images is less than 20, amplitude-based methods cannot reject non-homogeneous pixels. A new method is therefore introduced to accurately identify SHP pixels in small datasets.

Inspired by the principle of NL-SAR algorithm (Deledalle et al., 2015), we extend the general likelihood ratio (GLR) test to measure the similarity between two pixels over time series SAR data. For N co-registered multi-temporal SLC images, a N-dimensional complex scattering vector $\mathbf{Z}(x)$ ordered in acquisition dates can be formed at each pixel x as:

$$\mathbf{Z}(x) = [z_1(x), z_2(x), \cdots, z_N(x)]^T \tag{3}$$

where $z_i(x)$ ($i = 1,2, \ldots, N$) is the complex value of the ith image acquisition at pixel x and the superscript T stands for a transpose.

A special sample covariance matrix for pixel x is designed for the GLR test. The N-dimensional complex scattering vector $\mathbf{Z}(x)$ can be combined into $N / 2$ scattering vectors $\mathbf{S}(x)$ with two successive elements forming a pair by assuming N is an even number:

$$\mathbf{S}_k(x) = [z_j(x), z_{j+1}(x)]^T, k = 1, 2, \cdots, N/2; j = 2k - 1 \tag{4}$$

Then the initial covariance matrix can be estimated over samples of the same pixel taken along the temporal dimension as below:

$$\mathbf{C}(x) = \frac{2}{N} \sum_{k=1}^{N/2} \mathbf{S}_k(x) \mathbf{S}_k(x)^H \tag{5}$$

where the superscript H indicates a Hermitian transpose. The sample covariance matrix $\mathbf{C}(x)$ is a Hermitian positive definite matrix, and it follows a complex Wishart distribution with $N / 2$ degrees of freedom.

The logarithm for the GLR statistic under the assumption that x_1 and x_2 are similar can be expressed as (Conradsen et al., 2003):

$$\ln Q(\mathbf{C}_1, \mathbf{C}_2) = q(2N \ln 2 + \ln |\mathbf{C}_1| + \ln |\mathbf{C}_2| - 2 \ln |\mathbf{C}_1 + \mathbf{C}_2|) \tag{6}$$

where $\mathbf{C}_1$ and $\mathbf{C}_2$ are the sample covariance matrices for pixels x_1 and x_2, and $q = N / 2$. The larger the test statistic $\ln Q(\mathbf{C}_1, \mathbf{C}_2)$, the pixels x_1 and x_2 are more similar to each other. In general, the initial covariance matrices are calculated using equal q samples.

In order to decrease the variance of the test, the similarity is evaluated over small patches instead of single pixel (Deledalle et al., 2015). The similarity $\Delta(x_1, x_2)$ of two patches centered on pixels x_1 and x_2 is defined as:

$$\Delta(x_1, x_2) = \sum_{t=-p}^{p} - \ln Q(\mathbf{C}(x_1 + t), \mathbf{C}(x_2 + t)) \tag{7}$$

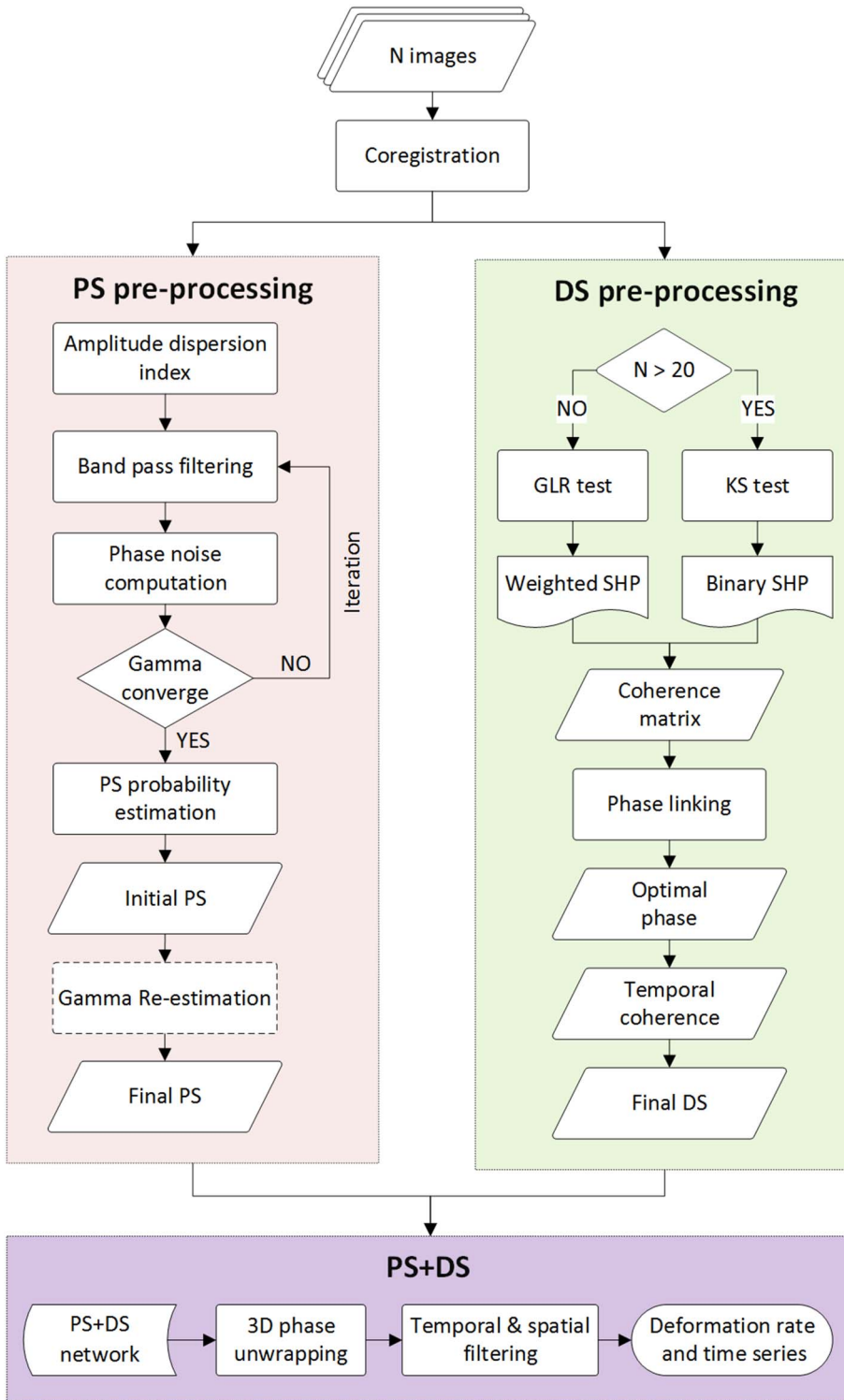where $t \in [-p,p]^2$ is a 2D shift indicating the location within each patch.

The kernel function proposed in NL-SAR is adopted to transform the similarities into corresponding weights (Deledalle et al., 2015):

$$\omega(x_1, x_2) = \begin{cases} \exp\left(-\frac{|G^{-1}\{F[\Delta(x_1,x_2)]\} - c|}{h}\right) & \text{if } x_1 \neq x_2 \\ 1 & \text{if } x_1 = x_2 \end{cases} \tag{8}$$

where F is the cumulative distribution function of $\Delta(x_1, x_2)$ under the assumption that x_1 and x_2 are subject to the same distribution, G^{-1} is the reciprocal of the chi-square distribution G with 49 degrees of freedom, c is the mathematical expectation of $G^{-1}\{F[\Delta(x_1, x_2)]\}$, and the filtering parameter h is usually set as $1/3$. The empirical cumulative distribution function F is unknown, but can be learned by sampling the patch similarities on a selected homogeneous pure-speckle area.

For each pixel x' in a fixed window Ω of size 25×25, centered on pixel x, the weight $\omega(x, x')$ can be obtained by applying this process. In general, the pixels with more than 20 SHPs are selected as DS candidates in order to preserve PS information (Ferretti et al., 2011). In our approach, only if the number of SHPs with high weights (e.g. > 0.5) in window Ω is larger than 20, then pixel x is selected as a DS candidate. A weighted averaging estimator is employed to calculate the complex coherence matrix for each DS candidate using the normalized complex scattering vectors $\mathbf{Y}(x')$ and their weights $\omega(x, x')$ in a search window:

$$\mathbf{T}_{\mathrm{GLR}}(x) = \frac{\sum\limits_{x' \in \Omega} \omega(x, x') \mathbf{Y}(x') \mathbf{Y}(x')^H}{\sum\limits_{x' \in \Omega} \omega(x, x')} \quad (9)$$

$$\mathbf{T}_{\mathrm{KS}}(x) = \frac{1}{N} \sum_{x' \in \Omega} \mathbf{Y}(x') \mathbf{Y}(x')^H \quad (10)$$

When the number of available images is large, the computation time cost of the GLR test increases significantly. An alternative method, e.g. KS test (Stephens, 1970), can be used to identify the SHP. Since the KS test requires a large number of samples (Jiang et al., 2015), it is used to identify the SHP set Ω for pixel x only when $N > 20$. The sample complex coherence matrix can be estimated as follows:

4.2.2. Estimation of the optimal phase

The optimal phase series of each pixel, $\boldsymbol{\theta} = [\theta_1, \theta_2, ..., \theta_N]^T$ can be estimated using the coherence matrix as calculated in Section 4.2.1. Without loss of generality, we set the first value of $\boldsymbol{\theta}$ as zero, i.e. $\theta_1 = 0$. The maximum likelihood estimation (MLE) of $\boldsymbol{\theta}$ is computed as follows:

$$\theta_{ML} = \underset{\theta}{\arg\max}\{\boldsymbol{\eta}^H(-|\mathbf{T}|^{-1}\circ\mathbf{T})\boldsymbol{\eta}\} \tag{11}$$

where $\boldsymbol{\eta} = [0, e^{j\theta_2}, \ldots, e^{j\theta_N}]^T$, and the symbol $\circ$ represents the mathematic operator of Hadamard product between two matrices obtained by Eq. (9) or Eq. (10). Here, we employ a phase linking approach (Monti Guarnieri and Tebaldini, 2008) to solve this equation, which can be expressed in a closed form as:

$$\hat{\theta}_n^k = \arg\left\{\sum_{m\neq n}^N \{|\mathbf{T}|^{-1}\}_{mn}\{\mathbf{T}\}_{mn}\exp(j\hat{\theta}_m^{k-1})\right\} \tag{12}$$

where k is the iteration step.

The quality of estimated optimal phases can be measured by the goodness of fit formulated as:

$$\gamma = \frac{2}{N^2 - N}\, \mathrm{Re}\sum_{m=1}^N\sum_{n=m+1}^N e^{j\phi_{mn}}e^{-j(\theta_m-\theta_n)} \tag{13}$$

where γ is the goodness of fit index, an extension of the temporal coherence (Ferretti et al., 2000), ϕ_{mn} is the phase value of the item at row m and column n of the coherence matrix, and θ_m and θ_n are the estimated optimal phases. The DS candidates will be further weeded according to the goodness of fit index. Only those candidates exhibiting a γ value higher than a predefined threshold will be selected as the final DS targets.

4.3. Combined analysis of PS and DS

The DS targets with estimated optimal phases are equivalent to quasi-PS targets. They can be combined with PS targets for further analysis using a standard PSI tool, as shown in the bottom block of Fig. 6. Here the StaMPS/PSInSAR processing program is used (Hooper et al., 2007). DS pixels that coincide with PS pixels are dropped. All the PS and DS pixels are connected to form the Delaunay triangulation network for phase analysis. The phase is firstly corrected for the spatially uncorrelated part of the look angle error due to the DEM error and pixel phase center uncertainty. The 3D phase unwrapping is then implemented to unwrap the interferometric phase in temporal and spatial dimensions (Hooper et al., 2012). Optionally, the unwrapped phases can be filtered by a high-pass filter in time and a low-pass filter in space to estimate the remaining spatial correlated nuisance terms, such as the atmospheric and orbital phase. Finally, the deformation rate and time series can be retrieved after subtracting above phase components (Hooper et al., 2007).

5. Performance evaluation of CSI

In this section, the performance of DS pre-processing including SHP identification and optimal phase estimation is first investigated. The accuracy of CSI method is then assessed by inter-comparison between different methods and different SAR datasets and evaluated against in-situ GPS measurements.

5.1. DS pre-processing

5.1.1. SHP identification

We compared the SHP identification capabilities of GLR test and KS test by changing the number of PALSAR images used. The river was selected as a homogenous area, as shown in the optical image from Google Earth™ in Fig. 7. The big red point located in the center of the PALSAR mean amplitude maps represents the reference pixel. The color indicates the level of similarity with blue and red colors corresponding to complete dissimilarity and similarity, respectively.

GLR test correctly assigned heterogeneous pixels with near-zero weights, and other pixels with nonzero values according to their similarity with respect to the reference pixel. In contrast, the KS test misclassified some heterogeneous pixels as SHP, particularly when the

number of images was small. The KS test is highly sensitive to the number of images, while the GLR test yields satisfactory results even for small datasets, such as six images. Therefore, we employed the GLR test to identify SHP pixels for small datasets, such as the PALSAR and ASAR data stacks used in this study.

5.1.2. Optimal phase estimation

The complex coherence matrices for DS pixels were computed using the identified SHP pixels. The optimal phase values of DS pixels were retrieved using the phase linking method described in Section 4.2.2. In principle, the adaptive estimation of the coherence matrix and the phase linking operation are equivalent to spatial and temporal adaptive filtering of the interferometric phases, respectively. Fig. 8 presents the original noisy, adaptively filtered, and unwrapped interferometric phase for the data pair of 27 June 2008 vs. 25 September 2007, zoomed on the Jiaju landslide. The phase noise was largely filtered, which makes phase unwrapping more accurate.

The goodness of fit index was computed using Eq. (13) on the optimal phase. The DS candidates were further selected by thresholding the goodness of fit index. In our experiment, for both PALSAR and ASAR datasets, only DS candidates exhibiting an index higher than 0.65 were kept for further time series analysis. The DS targets, combined with the PS points, are used to estimate the deformations, whose accuracy is evaluated by follows.

5.2. Accuracy assessment of CSI measurements

5.2.1. Consistency among PSI, SBAS and CSI measurements

The images covering the whole slope, larger than the Jiaju landslide, were processed for assessment purpose. Fig. 9 shows the maps of line-of-sight (LOS) deformation rates measured by PSI, SBAS, and CSI from PALSAR and ASAR data stacks, respectively. The deformation signals in the CSI-derived results are clearer than those estimated by PSI and SBAS methods. The spatial reference point was set at the location of GPS station G2.

The total number of MPs and corresponding spatial density detected by the three methods are listed in Table 2. As expected, the proposed CSI method identified many more MPs than either PSI or SBAS. For the PALSAR data stack, the number of MPs detected by CSI increased by about 15 and 10 times with respect to those obtained by PSI and SBAS separately. For the ASAR data stack, a similar pattern was observed with the corresponding increments being 25 and 10 times. Furthermore, the number of MPs detected by CSI and SBAS from PALSAR data was almost five times those derived from ASAR data, which might be attributed to the higher spatial resolution and less decorrelation for the L-band PALSAR data.

In order to assess the consistencies among the results obtained by PSI, SBAS and CSI, correlation analyses were carried out between each pair of deformation rate measurements produced by each of the three methods for both PALSAR and ASAR data. Fig. 10 shows bi-variable scatterplots for all six pairs. For each pair, only the common MPs are plotted and used for calculation of the Pearson correlation coefficients and the mean/standard deviation of differences between the results.

A few points can be inferred from Fig. 10. First, the correlation between PSI and SBAS was the highest for both data stacks, while CSI results show higher correlation with SBAS than with PSI. This pattern agrees well with the significant differences in MP detection capability among the three methods. Second, ASAR data yielded overall better consistency than PALSAR, which might be justified by the facts that the numbers of common MPs selected for ASAR data are much less than those for PALSAR. Most MPs for ASAR are more concentrated around the zero value than the MPs for PALSAR. Thirdly, some outliers can be clearly identified in the first two scatterplots of Fig. 10, as marked by the blue dashed ellipses. The existence of such outliers suggests that there is significant underestimation in the PSI-measured deformation rates for the PALSAR data when compared with SBAS and CSI results.
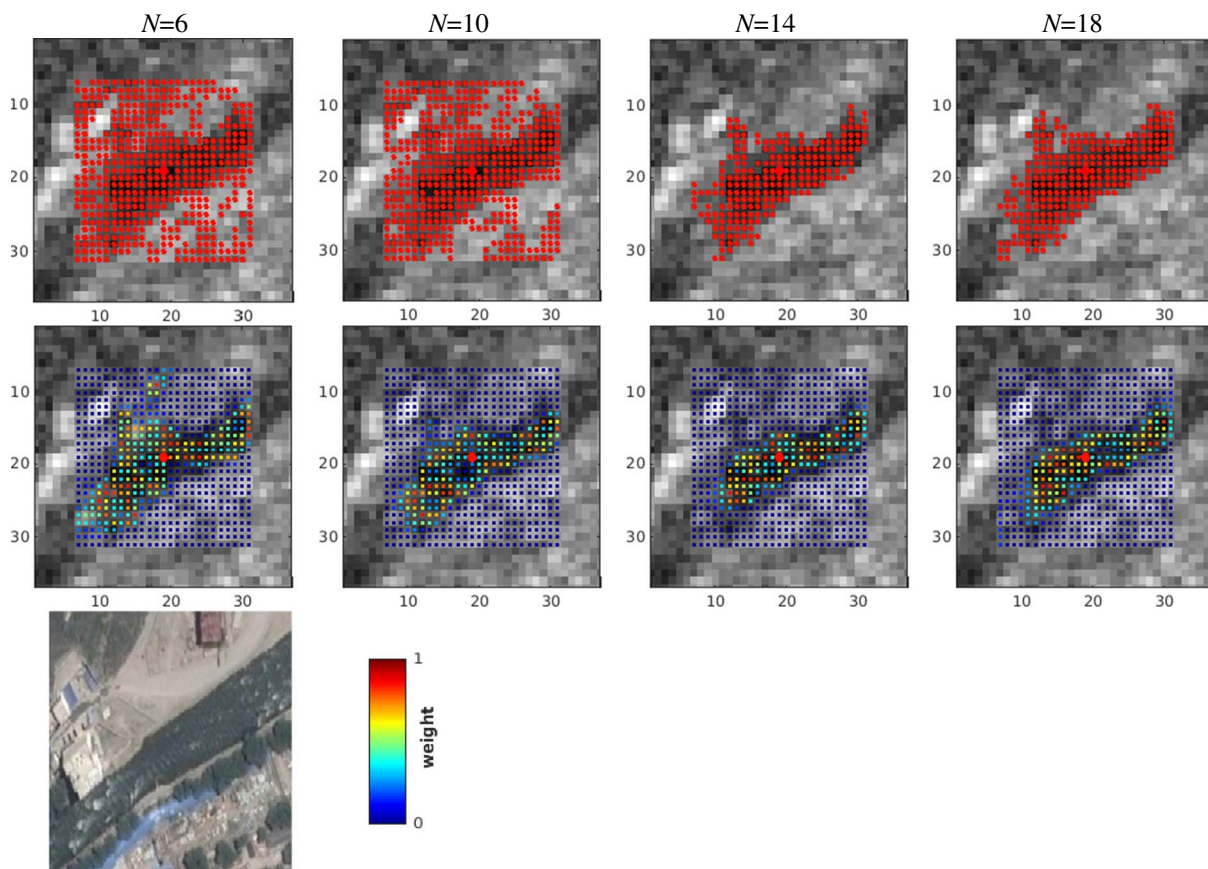
Fig. 7. Test of SHP identification with different number of images. First row: KS test, second row: GLR test, third row: corresponding optical image over the same area from Google Earth™. Blue color denotes complete dissimilarity, while red color indicates complete similarity, and other values represent similarity level between 0 and 1. (For interpretation of the references to color in this figure legend, the reader is referred to the web version of this article.)
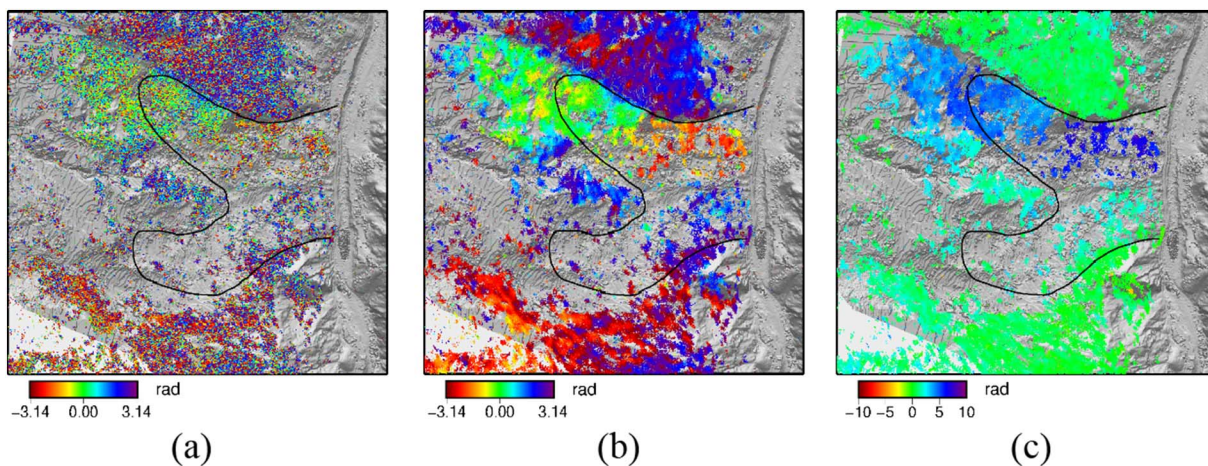

Fig. 8. The differential interferograms over the Jiaju landslide for the pair of 27 June 2008 vs. 25 September 2007, with a temporal interval of 276 days and a normal baseline of 584 m. (a) Noisy phase, (b) estimated optimal phase, and (c) unwrapped phase.

5.2.2. Cross-comparison between PALSAR and ASAR derived deformation rates

As revealed by Table 2 and Fig. 9(e) and (f), the proposed CSI method detected many more MPs from the PALSAR data stack than from ASAR, which clearly shows the big advantage of using L-band SAR data in landslide studies over C-band data owing to less decorrelation and deeper penetration capability into vegetation. Nevertheless, the results derived from both datasets show a generally similar spatial distribution pattern of active deformation areas. In order to check the inter-sensor consistency of deformation rate measurements, we carried out a cross-comparison of the CSI results for the PALSAR and ASAR datasets.

In consideration of the mismatch of MPs from the two datasets in geolocation due to dissimilar imaging geometries, we first unified them into a common geographic grid of one arc-second resolution by resampling and aggregation. In particular, the deformation rate value for each grid cell was calculated by averaging the MPs falling within it. The scatterplots of deformation rates derived from the two SAR datasets are given in Fig. 11(a), with a good correlation of 0.79. The root mean square error (RMSE) of the difference is 10.3 mm/year. Such a
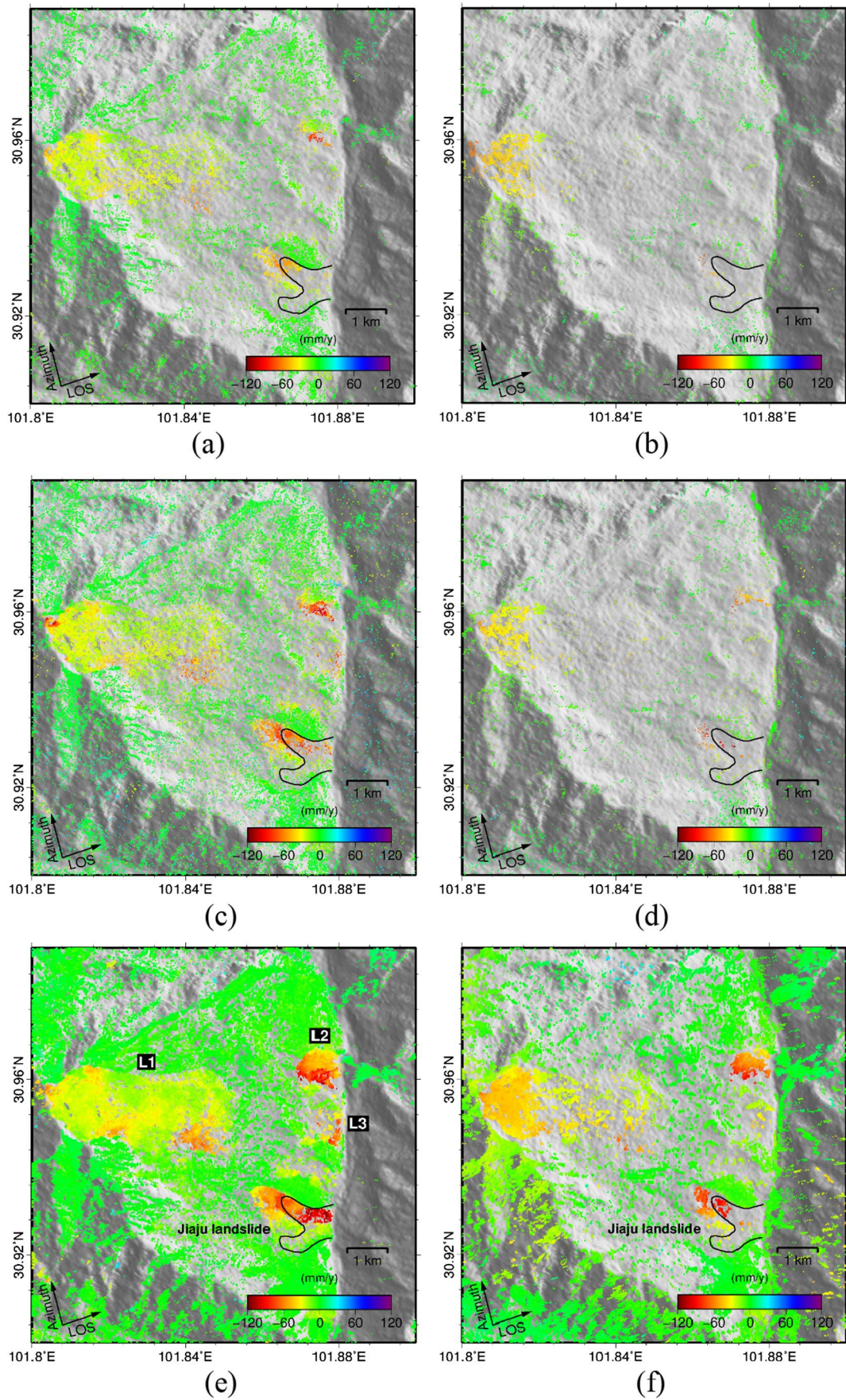
Fig. 9. The LOS deformation rates derived from both PALSAR (left column) and ASAR (right column) data using three different time series InSAR techniques. (a–b) PSI, (c–d) SBAS, and (e–f) CSI. The background image is the shaded ASTER GDEM.

Table 2
Number of MPs and their spatial density in the results of the three methods.

	Number of MPs		Spatial density (MPs/km^2)	
	PALSAR	ASAR	PALSAR	ASAR
PSI	30,902	4291	323	44
SBAS	47,559	10,298	498	107
CSI	474,368	104,281	4973	1093

difference may be caused by various factors such as inconsistent temporal coverage, different look angle, and data processing errors.

5.2.3. Validation of PALSAR-measured deformation rates using GPS measurements

To quantitatively evaluate the accuracy and reliability of CSI results, we performed comparisons between CSI-measured deformations from PALSAR data and GPS measurements on the Jiaju landslides. The three-dimensional (3D) GPS measurements were projected onto the PALSAR LOS direction to enable the comparison. For each GPS monitoring station, all the PALSAR measurement points located nearby with the horizontal distance to the GPS station ≤ 50 m were selected to calculate a mean displacement rate. This mean value was used as a proxy for comparison against GPS measurements. Fig. 11(b) presents a scatterplot of displacement rates measured by GPS and PALSAR data. These two kinds of measurements agree well with each other, showing a strong correlation of about 0.97. The RMSE of the difference was 10.5 mm/year.

In addition to correlation analysis of displacement rate measurements, we also compared the time series displacements measured by CSI from PALSAR data and GPS measurements. For each GPS

monitoring station, the spatially nearest PALSAR measurement point was taken for comparison. To ensure comparability, both time series of accumulative displacements were calibrated with respect to the corresponding PALSAR/GPS observations in the end of 2006. The calibrated displacement time series for all the GPS monitoring stations are plotted in Fig. 12, with the corresponding discrepancy in displacement rate reported. In general, both time series measurements match well with each other and show similar evolution trends at most stations.

More specifically, 13 out of the 20 monitoring stations exhibit discrepancies in the displacement rate between GPS and InSAR less than 10 mm/year, and four stations show discrepancies between 10 mm/year and 15 mm/year. Only three stations, i.e. G12, G18, and G22, have discrepancies larger than 15 mm/year. The smallest difference of −0.537 mm/year was found at station G8. In addition, the GPS observations for G3 seem unreliable since the time series displacements fluctuated extraordinarily, as shown by the first plot in Fig. 12.

The discrepancies between InSAR and GPS measurements may be attributed to a few factors. One is the spatial mismatch between the InSAR measurement points and the GPS stations. Since uneven displacements were detected over the Jiaju landslide as shown in Fig. 9, a distance of a few tens meters might cause significant variation of displacement measurements. Another key factor is the asynchronous observations by the two techniques along the temporal dimension. As revealed by Fig. 12, the temporal evolution of displacements is not a perfect linear procedure. Therefore, different observation periods and different temporal sampling schemes would inevitably result in discrepancy of displacement measurements.

In summary, overall good agreement between different InSAR methods, between different SAR datasets and between InSAR and GPS were obtained, which suggests that the proposed CSI method can achieve accurate and reliable surface displacement measurement for
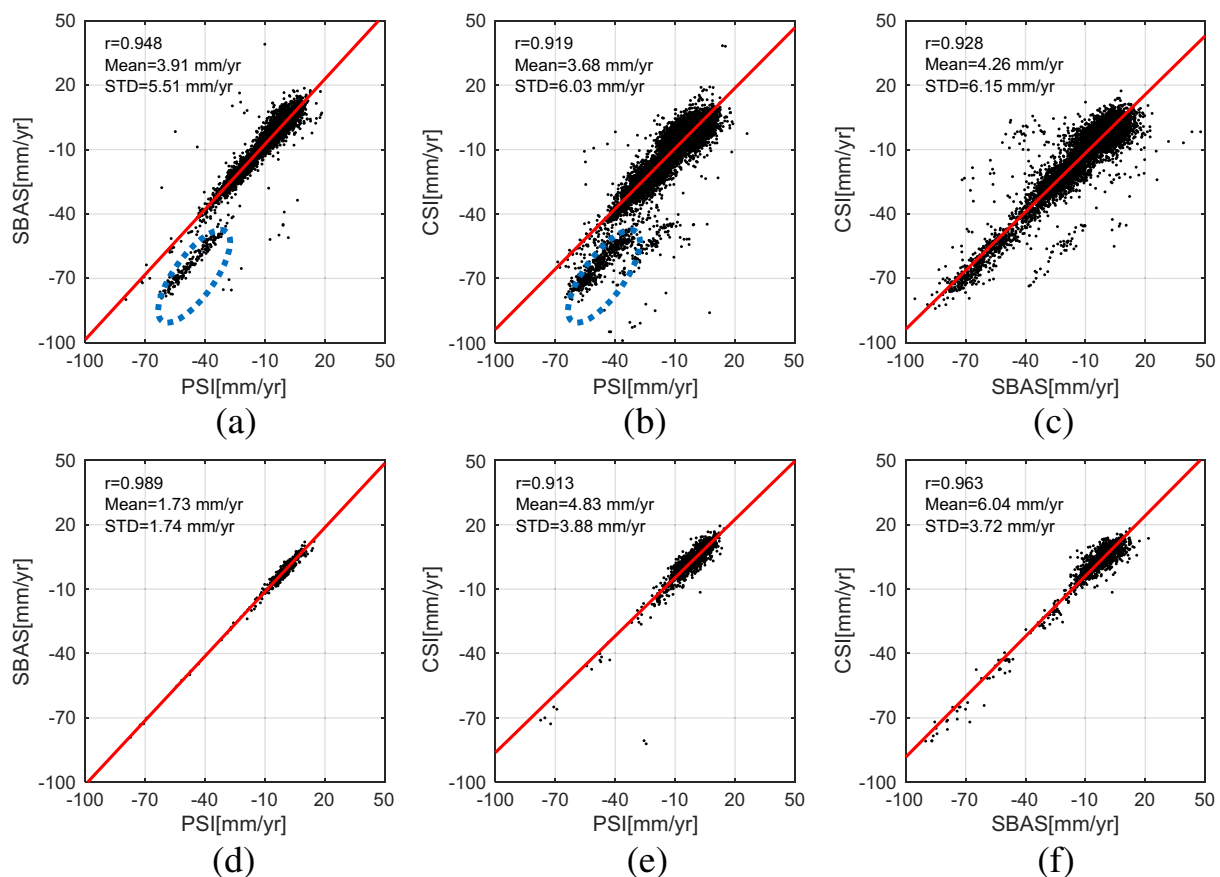

Fig. 10. Correlations between deformation rates measured by PSI, SBAS and CSI on the common MPs. (a–c) PALSAR dataset, and (d–f) ASAR dataset.
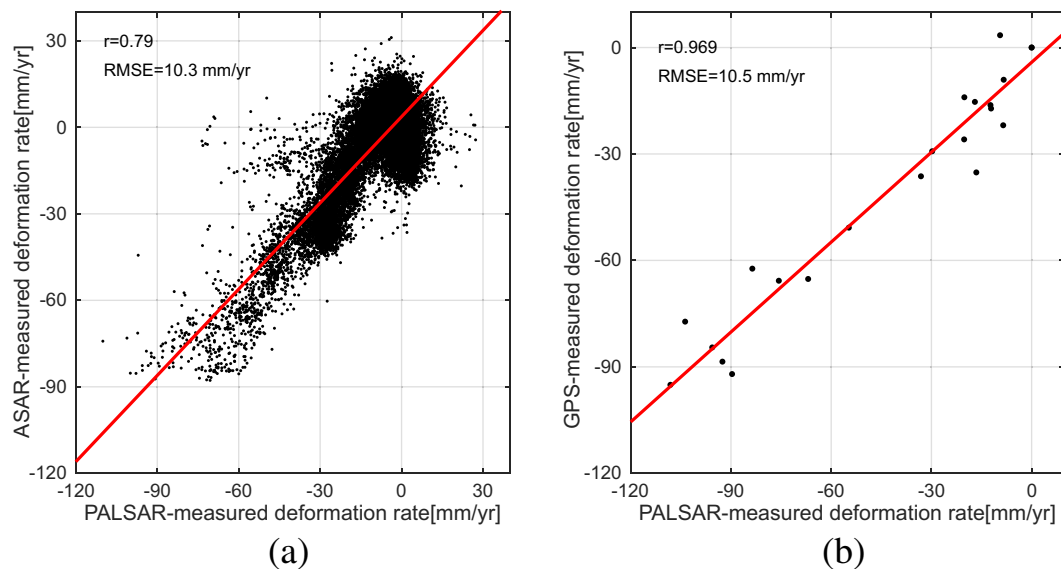
Fig. 11. Result validation. (a) Cross-comparison between PALSAR-measured and ASAR-measured deformation rates; (b) PALSAR-measured and GPS-measured deformation rates (right). The deformation rate of PALSAR is obtained by CSI method. The deformation of GPS measurements is projected on the LOS direction of PALSAR satellite. The deformations of PALSAR and ASAR are computed with respect to the GPS station G2.

landslides in mountainous areas. In contrast to GPS observations, the InSAR technique provides measurement points at much higher density, equivalent to thousands of GPS stations per km^2. The CSI method however, detects many more points than the two classical time series InSAR techniques, i.e. PSI and SBAS in rural environments.

6. Characterization of landslide deformation activities and related impact factors

The deformation rate maps in Fig. 9 show that there are actually four visibly unstable zones over the giant slope of Niexia Township, the L1, L2, L3, and Jiaju landslides. The L1 landslide had the largest sliding range from the summit to the hillside (circa 3000–4500 m a.s.l.), but with relatively slight motion. Due to inaccessibility and being far away from human settlements, this landslide has never drawn much attention before our study. According to our knowledge, the surface displacements of this landslide likely correspond to rock debris motion that was driven by seasonal snowmelt. The other three detected landslides were located at the slope foot near the provincial road S211 and Dajinchuan River. All of their maximum LOS deformation rates were larger than 100 mm/year. The deformation characteristics of the Jiaju landslide and impact factors for its instability are analyzed in detail in the following sections.

6.1. Deformation characteristics of the Jiaju landslide

The LOS deformation rates over the Jiaju landslide measured by PSI, SBAS, and CSI separately from the PALSAR data stack are illustrated in Fig. 13. Evidently, the PSI-derived MPs are so sparse that it was very difficult to identify the landslide range. Although the number of MPs from SBAS shows a slight increase, the displacements were obviously underestimated at the foot of the landslide with respect to the GPS measurements. The number of MPs detected by CSI increased by nearly ten times with more accurate deformation measurements than SBAS. The boundaries between the stable and unstable areas are more distinct. We can see from Fig. 13(c) that the northern part of the Jiaju landslide underwent strong displacements at a maximum rate of about 120 mm/year, while the southern part moved significantly slower at rates of 20–60 mm/year.

The CSI-derived deformation rate map allows us to update landslide boundaries determined by previous geological exploration. Fig. 14 plots

the deformation rates of MPs distributed along the profiles A–B and C–D, as marked by the black dashed lines in Fig. 13(c). The profile A–B stretches from the top to the toe of the northern part of the Jiaju landslide. Fig. 14(a) reveals that the area outside the old boundary (the gray line) defined by geological exploration was also moving, suggesting that the northwest boundary should be stepped outward by 580 m and upward by 200 m, with the new boundary indicated by the black line. The bottom region in the northern part of the landslide moved faster than the upper region. According to the local slope angle, we can divide the profile A–B into two sections separated by the red dashed line that corresponds to the location marked by the black arrow in Fig. 13(c). For the upper section with a mean slope angle of about 15°, the movement was distinctly slower than that in the lower section with a steeper slope angle of about 20°.

Another profile C–D crosses the landslide bottom from north to south, as shown in Fig. 13(c). A sudden jump of the displacement rates can be seen near the northern boundary of the Jiaju landslide, while no clear boundary can be found for the southern part. The magnitude of deformation decreased gradually from point C to D, but with a step around the middle of the dot-dash line, which corresponds to the border between the northern and southern parts of the landslide.

The spatial pattern of surface deformation is closely related to the slope of the sliding surface as shown by the engineering geological profiles in Fig. 3. The sliding surface of the northern part is steeper than that in the southern part, and the sliding surface of the front is steeper than that in the rear. Apparently, the steeper sliding surface had a higher possibility of incurring larger displacements. Therefore, the spatial pattern of surface displacements over the Jiaju landslide can be justified.

Fig. 15 renders time series LOS displacements over the Jiaju landslide measured by the proposed CSI method from PALSAR data stack, with respect to the first acquisition on 23 December 2006. Despite irregular temporal sampling by PALSAR data acquisitions, the process of spatial-temporal evolution of the Jiaju landslide was explicit, with an approximately linear deformation trend. The maximum accumulative displacement reached about 510 mm over the four-year period.

6.2. Impact factors for Jiaju landslide instability

As revealed by our analyses, the giant Jiaju landslide has undergone persistent active deformation during the long period from 2006 to
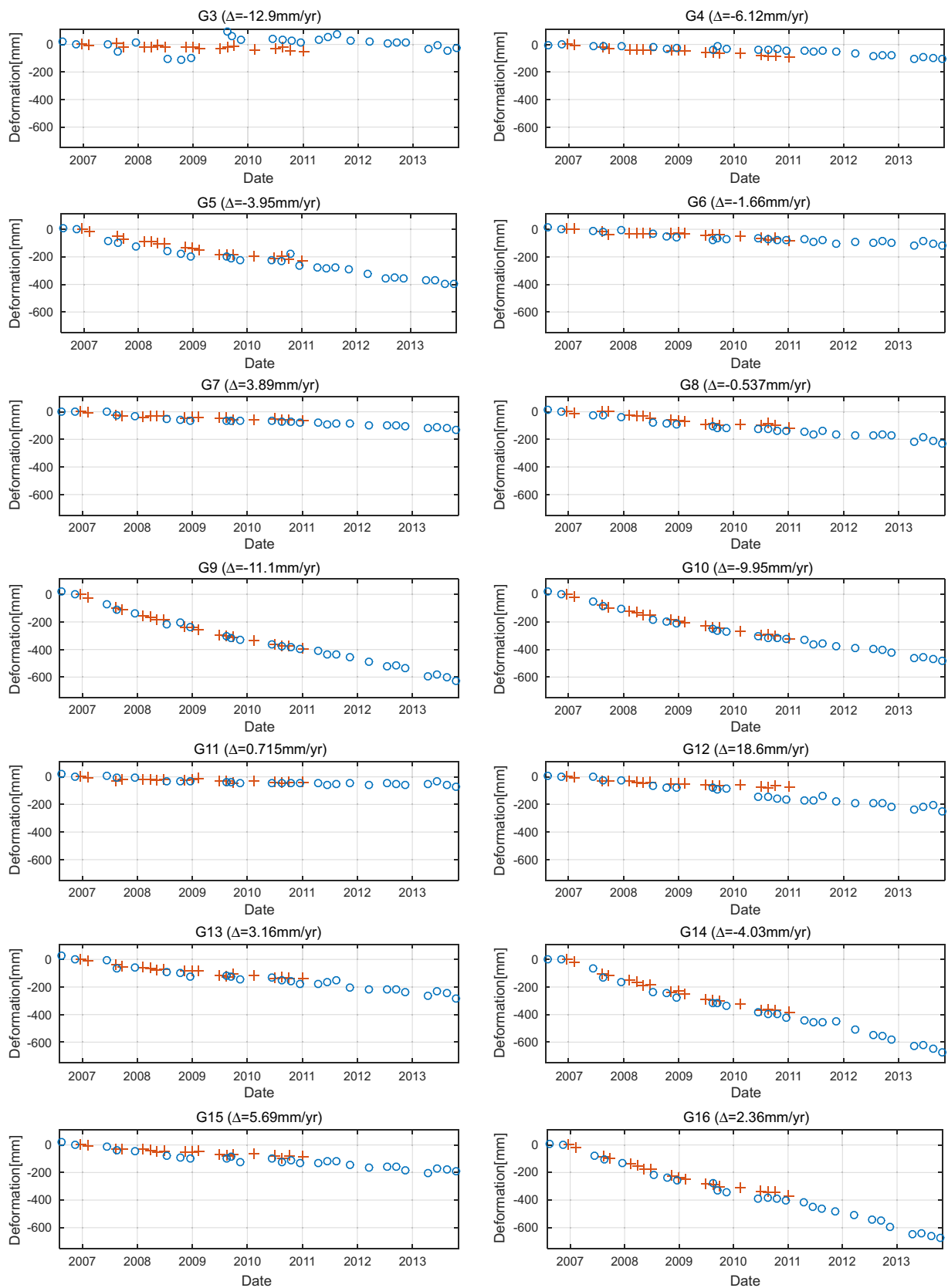
Fig. 12. Time series accumulative displacements measured at the 20 GPS monitoring stations. The GPS measurements were projected onto the PALSAR LOS direction. The red crosses and blue circles are PALSAR and GPS, respectively. (For interpretation of the references to color in this figure legend, the reader is referred to the web version of this article.)
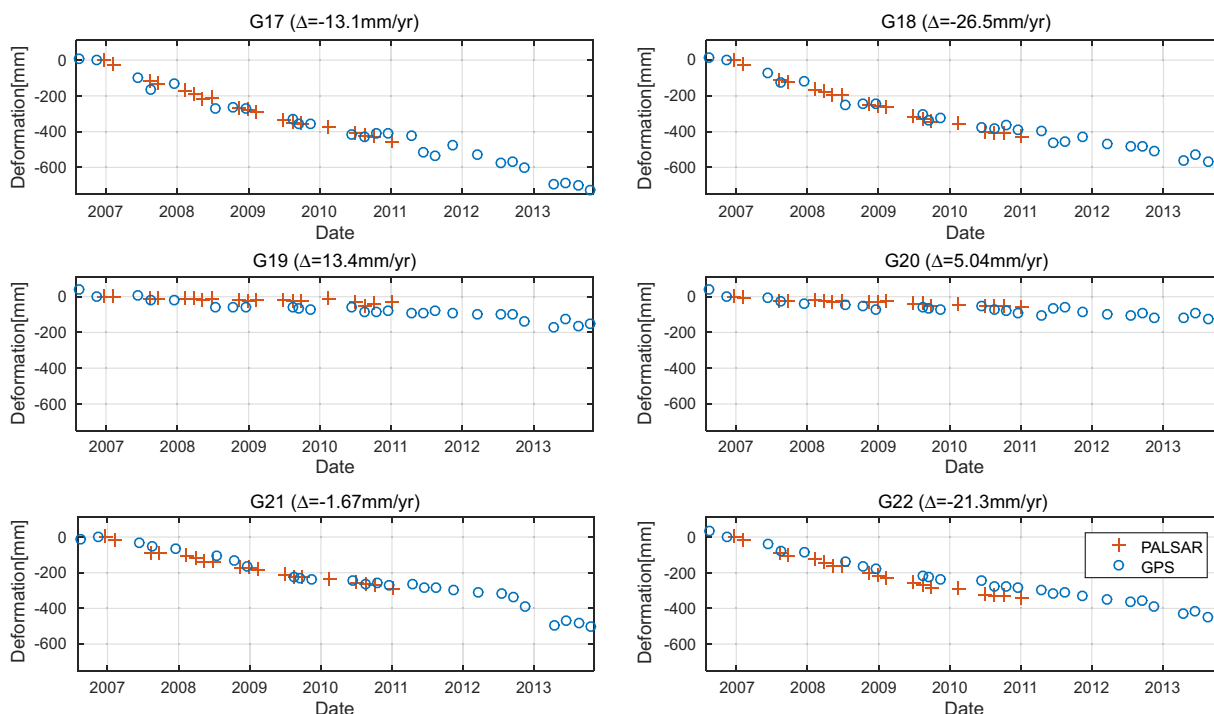
Fig. 12. (*continued*)

2013. Such a strong deformation might be affected by various factors including natural processes and anthropogenic activities. Here we sort out major driving factors and their impacts on the instability of the Jiaju landslide.

6.2.1. Rainfall and snowmelt

Although rainfall is recognized as the most important driving factor for the slope failure by changing groundwater level, this is not the case for the Jiaju landslide. As a typical Tibetan Plateau monsoon climate zone, Danba County has only a small annual mean rainfall no more than 600 mm. Hence, the impact of rainfall on the Jiaju landslide instability was limited. Nevertheless, the seasonal snowmelt on the summit together with rainfall may have contributed to the formation of three gullies on the landslide body. Water from these gullies infiltrates deposits composed of silty clay and gravelly soil, and softens soil of sliding zone mainly composed of silty clay and gravelly soil, and softens soil of sliding zone, likely causing local collapses and fissures.

6.2.2. Fluvial erosion

Actually, according to our field surveys, the predominant impact factor on the Jiaju landslide instability is fluvial erosion by the Dajinchuan River as shown in Fig. 16(a). During the flood season, the river water level may increase by nearly 5 m with respect to its normal status, with the peak flux exceeding 650 m³/s. The hydrodynamic pressure variations induced by the rapid river water level changes may lead to instability and movement at the front edge of the landslide.

The fluvial erosion is also likely attributed to the distinct shape of the river channel. As shown in Fig. 2, the cross section of Dajinchuan River at the foot of the Jiaju landslide is significantly smaller than both upstream and downstream, with the minimum width of 18 m being only about 1/3 of normal width. Such a bottleneck shape is prone to generate persistent and strong lateral fluvial erosion by the torrential water flow. Therefore, driven by the river erosion, the Jiaju landslide revived in the front, and then became active in the rear.

Furthermore, from Fig. 2 we can discern that there are distinct differences between the two sections of river channel beneath the front edges of Jiaju landslide in the northern and the southern parts. More specifically, the northern section is remarkably narrower than the

southern section, with the northern edge having a more convex shape than the southern edge. Such differences may produce stronger fluvial erosion on the northern part of landslide toe than in the southern toe, which might account for the faster deformation in the northern part.

6.2.3. Human activities

As several villages with thousands of local Tibetan residents are distributed over the slope upon which the Jiaju landslide is located, the influence of human activities on the landslide instability cannot be ignored. Anthropogenic disturbances are becoming more and more evident with flourishing rural tourism in Danba County over the past a few years, and must be taken into consideration when employing mitigation measures to reduce landslide hazards.

In general, the impact of human activities on the Jiaju landslide instability can be categorized into three types. First, the rapid village expansion with construction and renovation of numerous Tibetan-style buildings as well as some infrastructures like hillside roads to meet the demands of tourism development inevitably added huge loads to the landslide body. Moreover, during a field survey in April 2017 we saw tons of solid waste discharged at the rear part of the Jiaju landslide, as shown in Fig. 16(b), which could further increase dynamic loading, and thus destabilize the landslide.

Second, engineering works may change the surface geometry of the landslide toe. In particular, the Provincial Road S211 at the Jiaju section as a key transportation link was frequently damaged by the landslide deformation associated with fluvial erosion. Fig. 4(b) shows the road under renovation in May 2015. The road bed close to the river was partially destroyed by strong erosion. To reconstruct the road, the slope toe was excavated to get earth to fill the road foundation. Steep banks formed, creating more free faces at the slope toe, and thus the risk of failure under gravity was increased.

Thirdly, agricultural and forestry cultivation activities further destabilized the Jiaju landslide. There are many croplands and orchards around the villages, and irrigation is essentially needed to support the growth of crops and trees. However, when irrigated water infiltrates into the soil, only a small percentage can usually be absorbed by the plants, while the remainder will go deeper into the groundwater layer. Such a change of groundwater level induced by intensive irrigation can
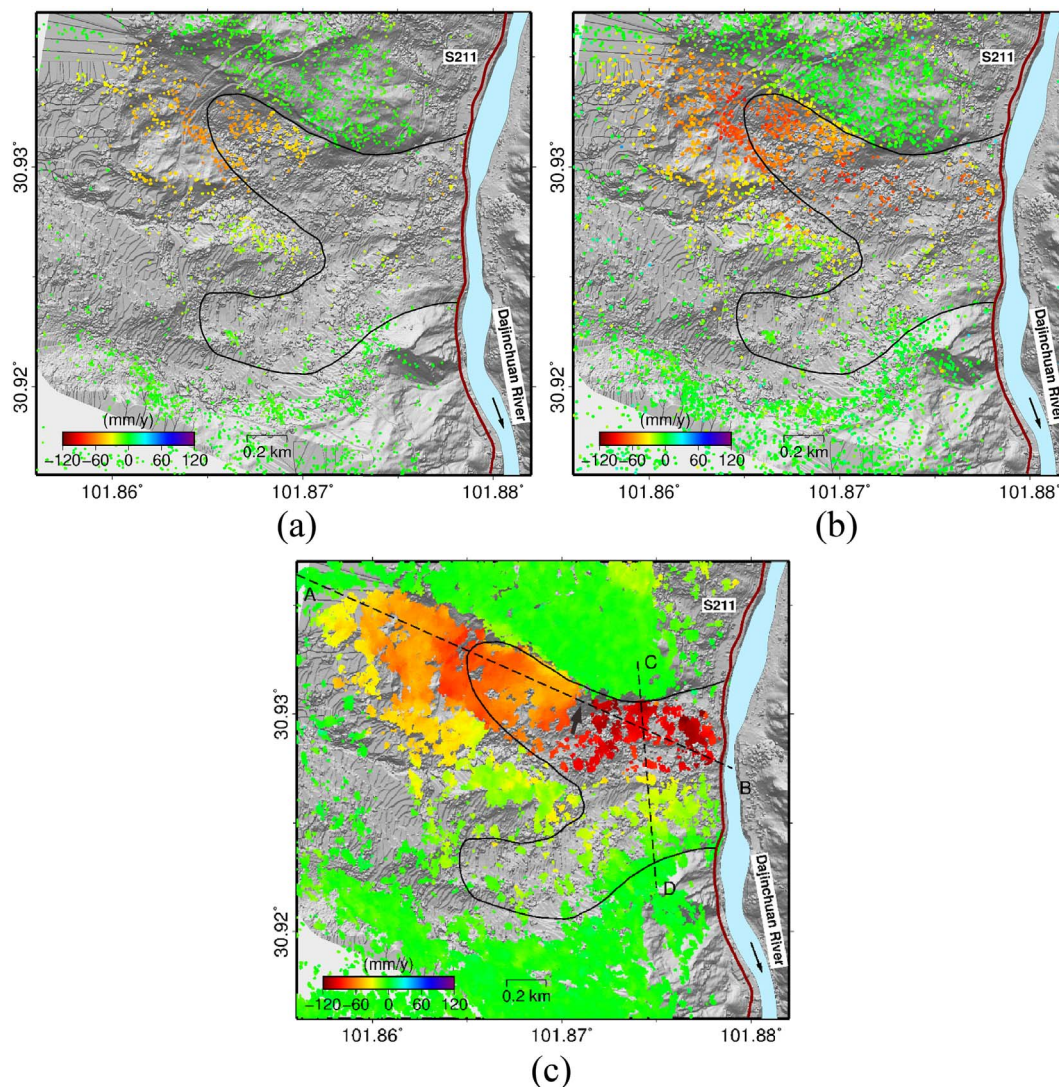
Fig. 13. The LOS deformation rates of Jiaju landslide from PALSAR measured by (a) PSI, (b) SBAS and (c) CSI. The dashed lines A–B and C–D in (c) indicate the profile lines in Fig. 14. The background is the same as that in Fig. 2.

be more significant than that due to rainfall, which might cause landslide deformation in local areas.

7. Discussion

In an application of time series InSAR techniques for landslide investigation over steep and forested terrain, the low spatial density of detectable coherent points generally results in phase unwrapping errors and consequently big uncertainties in the deformation measurements. The proposed coherent scatterers InSAR (CSI) approach jointly utilizes both persistent and distributed scatterers to increase the number of measurement points, with a special pre-processing strategy implemented for DS target identification and optimal phase estimation. The significantly increased MP density effectively improved deformation measurements by reducing phase unwrapping errors and raising the measurable spatial gradient of deformation. It also allowed us to delineate and update landslide boundaries more accurately. In particular, by using CSI our capability to detect potential landslides is substantially enhanced, since small unstable slopes that can hardly be detected by traditional time series InSAR analyses are also identified with CSI.

Regardless of the strengths of CSI method, the pre-processing of DS targets is time consuming. The computational time cost for the CSI

method is approximately five times of that for traditional time series InSAR approaches, which constitutes a major bottleneck for its application. For a single landslide, the computational expense is still acceptable. However, for landslide investigations across wide areas, the time cost of CSI analyses may increase to an extremely high level, and thus how to improve the computational efficiency by adopting the modern massively parallel computation technologies such as the general purpose graphics processing unit (GPGPU) has become a critical problem to be solved. On the other hand, DS pre-processing requires huge memory and disk storage space to hold intermediate data. According to our experiments, the storage space requirements for CSI are around four times of that needed by the standard PSI procedure. Therefore, another key problem worth investigation is how to optimize the CSI algorithm, especially the DS pre-processing procedure, to substantially reduce the consumption of storage space.

Apart from InSAR methods, SAR data plays another key role in InSAR-based landslide investigation. In our study, only medium-resolution PALSAR and ASAR datasets were processed. It is expected that the CSI method can benefit from the use of high-resolution SAR data acquired by satellites such as TerraSAR-X, COSMO-SkyMed and RADARSAT-2. The large volume of high-resolution SAR data however, will challenge CSI analyses.

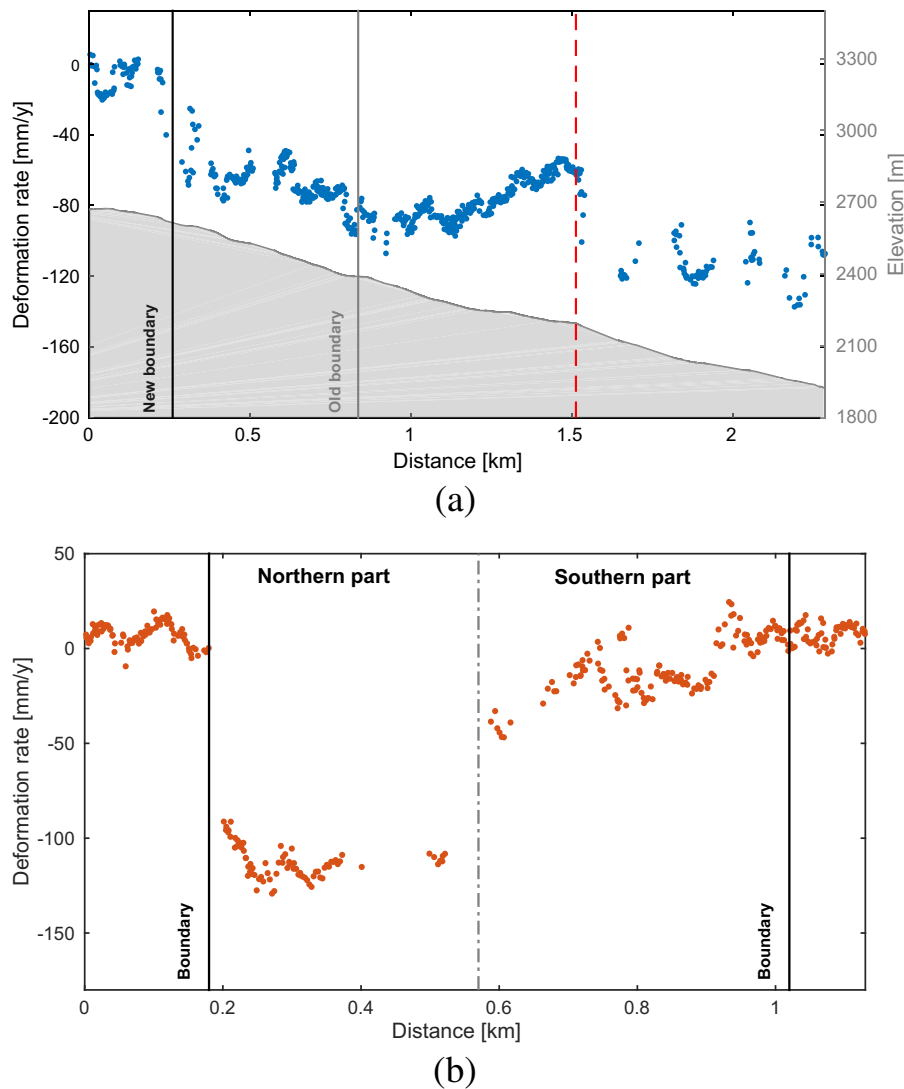Another challenge for the application of CSI method comes from the

operation of new-generation Sentinel-1 constellation of twin C-band SAR satellites. As the first fully operational satellite SAR mission, Sentinel-1 offers unprecedented earth observation capability with more frequent acquisition, more systematic wide-area coverage, better orbital control, and a totally free and open data policy. Undoubtedly, it will revolutionize the application of InSAR in landslide studies, with possible applications in wide-area detection of potential slope instabilities and early warnings of specific landslide disasters. Nonetheless, the huge data volume associated with the rapid creation and accumulation of SAR data archives will demand far more powerful InSAR data processing systems. Massive parallelization of the CSI method to meet the requirements of Sentinel-1 InSAR data analyses is highly desired. In addition, a sequential estimation scheme may be integrated into the CSI procedure to implement near real-time processing of the emerging SAR big data.

8. Conclusions

In this study, a new approach of multi-temporal InSAR analysis named CSI is proposed for mapping landslide surface displacements in rural or vegetated environments. The CSI method jointly utilizes targets of persistent and distributed scatterers to establish a much denser observation network to perform more reliable phase unwrapping so as to obtain more accurate displacement measurements than conventional time series InSAR approaches. In particular, two algorithms were

employed in the pre-processing of DS targets. The GLR test was adopted as an alternative to the KS test to robustly identify SHP pixels from small SAR data stacks. A phase linking approach was used to estimate the optimal phase values of DS targets.

To evaluate the effectiveness of the proposed CSI method, we applied it to detect historical displacements of the Jiaju landslide in Danba County, southwest China from two SAR data stacks of 19 ALOS PALSAR images and nine ENVISAT ASAR images. Comparisons among multiple displacement measurements derived by PSI, SBAS and CSI from both data stacks were carried out to evaluate their consistency. The CSI results derived from PALSAR data were further validated against in-situ GPS measurements. Finally, the spatial-temporal characteristics of Jiaju landslide deformation and related possible impact factors were analyzed. Our major findings derived from these experimental results can be summarized as follows.

First, the proposed CSI method as well as traditional PSI and SBAS methods yielded similar spatial distribution pattern of surface displacement rates. However, CSI detected much more MPs (> 10 times) than the other two methods in vegetated mountainous areas, which obviously benefits from the use of DS targets. Therefore, more details of the Jiaju landslide displacement field can be revealed by the CSI results, and the critical problem of displacement rate underestimation due to MP sparsity can be effectively overcome.

Second, although CSI results derived from PALSAR and ASAR data agreed well with each other in the identification of major active
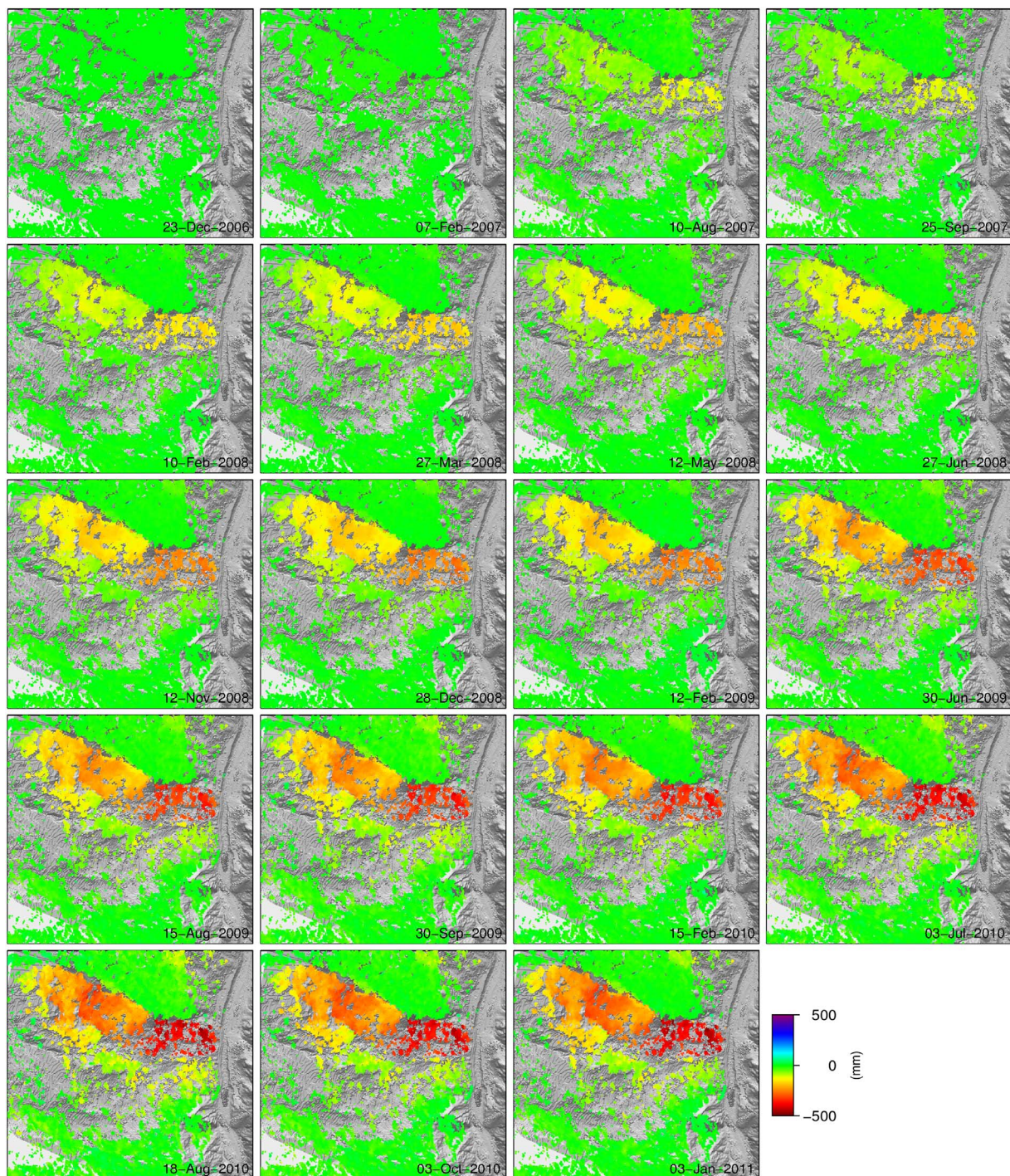
Fig. 15. The time series LOS displacement maps estimated from PALSAR datasets for Jiaju landslide. The acquisition on 23 December 2006 is set as the reference image.

deformation areas, the number of MPs detected from PALSAR data was almost five times of those derived from ASAR data, showing the big advantage of L-band SAR data over C-band data for landslide investigation in rural mountainous areas.

Thirdly, comparisons between CSI and GPS measurements show that an accuracy of about 10.5 mm/year was achieved by the CSI results for PALSAR data. This suggests that the CSI method has great potential to become a reliable tool to complement traditional geodetic techniques for landslide deformation monitoring.

Fourthly, the spatial-temporal characteristics of surface displacements over the Jiaju landslide were analyzed in details. An uneven deformation pattern was clearly disclosed by the CSI results derived

from PALSAR data, with the maximum LOS displacement rate being about 120 mm/year. Specifically, the northern part moves much faster than the southern part, and in the northern part the landslide toe moves faster than the rear. Furthermore, we delineated a new upper boundary for the northern part by identifying the sliding range of Jiaju landslide from the displacement rate map.

Finally, various impact factors for the Jiaju landslide instability were qualitatively investigated. According to our field surveys and analyses, the fluvial erosion by the Dajinchuan River was identified as the predominant driving factor for the deformation at the landslide toe, while the big difference in deformation rate between northern and southern parts can be largely attributed to the disparity in erosion

Fig. 16. Photos taken during field surveys. (a) The Dajinchuan River at the foot of the Jiaju landslide (May 2015); (b) Waste soil dumped at the rear part of the Jiaju landslide (April 2017).

(a)   (b)

strength due to dissimilar shape and orientation of river channel sections.

Using the active Jiaju landslide as an example, we have demonstrated the great potential of the proposed CSI method for landslide investigations in rural mountainous environments. Nevertheless, in order to face the big challenges brought by the new-generation operational satellite SAR systems empowered with innovative technologies, such as the Sentinel-1 in orbit and the TanDEM-L in development, we must carry out more in-depth studies to tackle key issues including substantial improvement of computational efficiency via algorithm optimization and parallelization, integration with other SAR remote sensing techniques for landslide monitoring in complicated rural environments, and 3D landslide surface displacement estimation by joint analyses of multi-source SAR datasets.

Acknowledgments

References

Bamler, R., Hartl, P., 1998. Synthetic aperture radar interferometry. Inverse Prob. 14 (4), R1–R54.

Berardino, P., Fornaro, G., Lanari, R., Sansosti, E., 2002. A new algorithm for surface deformation monitoring based on small baseline differential SAR interferograms. IEEE Trans. Geosci. Remote Sens. 40 (11), 2375–2383.

Biggs, J., Wright, T., Lu, Z., Parsons, B., 2007. Multi-interferogram method for measuring interseismic deformation: Denali Fault, Alaska. Geophys. J. Int. 170, 1165–1179.

Bovenga, F., Refice, A., Nutricato, R., Guerriero, L., Chiaradia, M., 2004. SPINUA: a flexible processing chain for ERS/ENVISAT long term interferometry. In: Proceedings of ESA-ENVISAT Symposium, Salzburg, Austria, pp. 6–10.

Bovenga, F., Nutricato, R., Refice, A., Wasowski, J., 2006. Application of multi-temporal differential interferometry to slope instability detection in urban/peri-urban areas. Eng. Geol. 88, 218–239.

Cao, N., Lee, H., Jung, H.C., 2015. A phase-decomposition-based PSInSAR processing method. IEEE Trans. Geosci. Remote Sens. 54 (2), 1074–1090.

Casu, F., Manzo, M., Lanari, R., 2006. A quantitative assessment of the SBAS algorithm performance for surface deformation retrieval from DInSAR data. Remote Sens. Environ. 102, 195–210.

Chen, N.S., Li, T.C., Gao, Y.C., 2005. A great disastrous debris flow on 11 July 2003 in Shuikazi valley, Danba County, western Sichuan, China. Landslides 2, 71–74.

Colesanti, C., Wasowski, J., 2006. Investigating landslides with space-borne Synthetic Aperture Radar (SAR) interferometry. Eng. Geol. 88, 173–199.

Colesanti, C., Ferretti, A., Prati, C., Rocca, F., 2003. Monitoring landslides and tectonic motions with the Permanent Scatterers Technique. Eng. Geol. 68, 3–14.

Confuorto, P., Di Martire, D., Centolanza, G., Iglesias, R., Mallorqui, J.J., Novellino, A., Plank, S., Ramondini, M., Thuro, K., Calcaterra, D., 2017. Post-failure evolution analysis of a rainfall-triggered landslide by multi-temporal interferometry SAR approaches integrated with geotechnical analysis. Remote Sens. Environ. 188, 51–72.

Conradsen, K., Nielsen, A.A., Schou, J., Skriver, H., 2003. A test statistic in the complex Wishart distribution and its application to change detection in polarimetric SAR data. IEEE Trans. Geosci. Remote Sens. 41 (1), 4–19.

Costantini, M., Falco, S., Malvarosa, F., Minati, F., 2008. A new method for identification and analysis of persistent scatterers in series of SAR images. In: Proceedings of IEEE International Geoscience and Remote Sensing Symposium 2008, pp. 449–452.

Costantini, M., Falco, S., Malvarosa, F., Minati, F., Trillo, F., Vecchioli, F., 2014. Persistent scatterer pair interferometry: approach and application to COSMO-SkyMed SAR data. IEEE J. Sel. Top. Appl. Earth Obs. Remote Sens. 7, 2869–2879.

Costantini, M., Ferretti, A., Minati, F., Falco, S., Trillo, F., Colombo, D., Novali, F., Malvarosa, F., Mammone, C., Vecchioli, F., Rucci, A., Fumagalli, A., Allievi, J., Ciminelli, M.G., Costabile, S., 2017. Analysis of surface deformations over the whole Italian territory by interferometric processing of ERS, Envisat and COSMO-SkyMed radar data. Remote Sens. Environ. http://dx.doi.org/10.1016/j.rse.2017.07.017. (in press).

Crosetto, M., Biescas, E., Duro, J., Closa, J., Arnaud, A., 2008. Generation of advanced ERS and Envisat interferometric SAR products using the stable point network technique. Photogramm. Eng. Remote. Sens. 74, 443–450.

Deledalle, C.A., Denis, L., Tupin, F., Reigber, A., Jäger, M., 2015. NL-SAR: a unified nonlocal framework for resolution-preserving (Pol)(In)SAR denoising. IEEE Trans. Geosci. Remote Sens. 53, 2021–2038.

Deng, G., Zheng, W., Yang, G., Liu, Y., Zhang, Q., Chen, Q., Tang, Y., 2011. GPS monitoring of the Jiaju landslide in Danba, Sichuan. Sediment. Geol. Tethyan Geol. 31, 99–104.

Deng, H., Wu, L., Huang, R., Guo, X., He, Q., 2017. Formation of the Siwanli ancient landslide in the Dadu River, China. Landslides 14, 385–394.

Di Martire, D., Paci, M., Confuorto, P., Costabile, S., Guastaferro, F., Verta, A., Calcaterra, D., 2017. A nation-wide system for landslide mapping and risk management in Italy: the second Not-ordinary Plan of Environmental Remote Sensing. Int. J. Appl. Earth Obs. Geoinf. 63, 143–157.

Du, Z., Ge, L., Li, X., Ng, A., 2016. Subsidence monitoring over the southern coalfield, Australia using both L-band and C-band SAR time series analysis. Remote Sens. 8, 543.

Eriksen, H.Ø., Lauknes, T.R., Larsen, Y., Corner, G.D., Bergh, S.G., Dehls, J., Kierulf, H.P., 2017. Visualizing and interpreting surface displacement patterns on unstable slopes using multi-geometry satellite SAR interferometry (2D InSAR). Remote Sens. Environ. 191, 297–312.

Ferretti, A., Prati, C., Rocca, F., 2000. Nonlinear subsidence rate estimation using permanent scatterers in differential SAR interferometry. IEEE Trans. Geosci. Remote Sens. 38, 2202–2212.

Ferretti, A., Prati, C., Rocca, F., 2001. Permanent scatterers in SAR interferometry. IEEE Trans. Geosci. Remote Sens. 39, 8–20.

Ferretti, A., Fumagalli, A., Novali, F., Prati, C., Rocca, F., Rucci, A., 2011. A new algorithm for processing interferometric data-stacks: SqueeSAR. IEEE Trans. Geosci. Remote Sens. 49, 3460–3470.

Fletcherwrited, R., 1981. Practical Methods of Optimization. J. Wiley.

Fornaro, G., Verde, S., Reale, D., Pauciullo, A., 2015. CAESAR: an approach based on covariance matrix decomposition to improve multibaseline–multitemporal interferometric SAR processing. IEEE Trans. Geosci. Remote Sens. 53, 2050–2065.

Fruneau, B., Achache, J., Delacourt, C., 1996. Observation and modelling of the Saint-Étienne-de-Tinée landslide using SAR interferometry. Tectonophysics 265, 181–190.

Fujisada, H., Bailey, G.B., Kelly, G.G., Hara, S., Abrams, M.J., 2005. ASTER DEM performance. IEEE Trans. Geosci. Remote Sens. 43, 2707–2714.

Gabriel, A.K., Goldstein, R.M., Zebker, H.A., 1989. Mapping small elevation changes over large areas: differential radar interferometry. J. Geophys. Res. Solid Earth 94, 9183–9191.

Ge, L., Ng, A.H.-M., Li, X., Abidin, H.Z., Gumilar, I., 2014. Land subsidence characteristics of Bandung Basin as revealed by ENVISAT ASAR and ALOS PALSAR interferometry. Remote Sens. Environ. 154, 46–60.

Hilley, G.E., Bürgmann, R., Ferretti, A., Novali, F., Rocca, F., 2004. Dynamics of slow-moving landslides from permanent scatterer analysis. Science 304, 1952–1955.

Hooper, A., 2008. A multi-temporal InSAR method incorporating both persistent scatterer and small baseline approaches. Geophys. Res. Lett. 35, 96–106.

Hooper, A., Zebker, H., Segall, P., Kampes, B., 2004. A new method for measuring deformation on volcanoes and other natural terrains using InSAR persistent scatterers. Geophys. Res. Lett. 31, 1–5.

Hooper, A., Segall, P., Zebker, H., 2007. Persistent scatterer InSAR for crustal deformation analysis, with application to Volcán Alcedo, Galápagos. J. Geophys. Res. Solid Earth 112, B07407–07401.

Hooper, A., Bekaert, D., Spaans, K., Arıkan, M., 2012. Recent advances in SAR interferometry time series analysis for measuring crustal deformation. Tectonophysics 514, 1–13.

Huang, R., 2009. Some catastrophic landslides since the twentieth century in the southwest of China. Landslides 6, 69–81.

Iglesias, R., Mallorqui, J., Monells, D., López-Martínez, C., Fabregas, X., Aguasca, A., Gili, J., Corominas, J., 2015. PSI deformation map retrieval by means of temporal sublook coherence on reduced sets of SAR images. Remote Sens. 7, 530.

Jiang, M., Ding, X., Hanssen, R.F., Malhotra, R., Chang, L., 2015. Fast statistically homogeneous pixel selection for covariance matrix estimation for multitemporal InSAR. IEEE Trans. Geosci. Remote Sens. 53, 1213–1224.

Kampes, B., 2006. Radar Interferometry: Persistent Scatterer Technique. Springer.

Kuehn, F., Albiol, D., Cooksley, G., Duro, J., Granda, J., Haas, S., Hoffmann-Rothe, A., Murdohardono, D., 2010. Detection of land subsidence in Semarang, Indonesia, using stable points network (SPN) technique. Environ. Earth Sci. 60, 909–921.

Lanari, R., Mora, O., Manunta, M., Mallorquí, J.J., Berardino, P., Sansosti, E., 2004. A small-baseline approach for investigating deformations on full-resolution differential SAR interferograms. IEEE Trans. Geosci. Remote Sens. 42, 1377–1386.

Lv, X., Yazıcı, B., Zeghal, M., Bennett, V., 2014. Joint-scatterer processing for time-series InSAR. IEEE Trans. Geosci. Remote Sens. 52, 7205–7221.

Massonnet, D., Feigl, K., 1998. Radar interferometry and its application to changes in the Earth's surface. Rev. Geophys. 36, 441–500.

Monti Guarnieri, A., Tebaldini, S., 2008. On the exploitation of target statistics for SAR interferometry applications. IEEE Trans. Geosci. Remote Sens. 46, 3436–3443.

Mora, O., Mallorqui, J.J., Broquetas, A., 2003. Linear and nonlinear terrain deformation maps from a reduced set of interferometric SAR images. IEEE Trans. Geosci. Remote Sens. 41, 2243–2253.

Ng, A., Ge, L., Li, X., Zhang, K., 2012. Monitoring ground deformation in Beijing, China with persistent scatterer SAR interferometry. J. Geod. 86, 375–392.

Ng, A., Ge, L., Li, X., 2015. Assessments of land subsidence in the Gippsland Basin of Australia using ALOS PALSAR data. Remote Sens. Environ. 159, 86–101.

Parizzi, A., Brcic, R., 2011. Adaptive InSAR stack multilooking exploiting amplitude statistics: a comparison between different techniques and practical results. IEEE Geosci. Remote Sens. Lett. 8, 441–445.

Perissin, D., Wang, T., 2012. Repeat-pass SAR interferometry with partially coherent targets. IEEE Trans. Geosci. Remote Sens. 50, 271–280.

Rosen, P., Hensley, S., Joughin, I., Li, F., Madsen, S., Rodriguez, E., Goldstein, R., 2000. Synthetic aperture radar interferometry. Proc. IEEE 88, 333–382.

Schmidt, D., Bürgmann, R., 2003. Time-dependent land uplift and subsidence in the Santa Clara valley, California, from a large interferometric synthetic aperture radar data set. J. Geophys. Res. Solid Earth 108.

Shi, X., Liao, M., Li, M., Zhang, L., Cunningham, C., 2016. Wide-area landslide deformation mapping with multi-path ALOS PALSAR data stacks: a case study of Three Gorges Area, China. Remote Sens. 8.

Simons, M., Rosen, P., 2007. Interferometric synthetic aperture radar geodesy. In: Schubert, Gerald (Ed.), Treatise on Geophysics. Elsevier, Amsterdam, pp. 391–446.

Stephens, M., 1970. Use of the Kolmogorov-Smirnov, Cramer-von Mises and related statistics without extensive tables. J. R. Stat. Soc. 32 (1), 115–122.

Wasowski, J., Bovenga, F., 2014. Investigating landslides and unstable slopes with satellite multi temporal interferometry: current issues and future perspectives. Eng. Geol. 174, 103–138.

Werner, C., Wegmuller, U., Strozzi, T., Wiesmann, A., 2003. Interferometric point target analysis for deformation mapping. In: Proceedings of IEEE International Geoscience and Remote Sensing Symposium 2003, pp. 4362–4364.

Yin, Y., Li, T., Tang, J., 2008. Landslide reactivation and emergency stabilization on Danba county town in Sichuan province. Chin. J. Rock Mech. Eng. 27, 971–978.

Yin, Y., Zheng, W., Liu, Y., Zhang, J., Li, X., 2010. Integration of GPS with InSAR to monitoring of the Jiaju landslide in Sichuan, China. Landslides 7, 359–365.

Zebker, H.A., Villasenor, J., 1992. Decorrelation in interferometric radar echoes. IEEE Trans. Geosci. Remote Sens. 30, 950–959.

Zhang, L., Ding, X., Lu, Z., 2011. Ground settlement monitoring based on temporally coherent points between two SAR acquisitions. ISPRS J. Photogramm. Remote Sens. 66, 146–152.

Zhang, L., Lu, Z., Ding, X., Jung, H.-S., Feng, G., Lee, C., 2012. Mapping ground surface deformation using temporally coherent point SAR interferometry: application to Los Angeles Basin. Remote Sens. Environ. 117, 429–439.